PKM2 diverts glycolytic flux in dependence on formate overflow

Mohaned Benzarti[1,2], Anais Oudin[3], Elodie Viry[4], Ernesto Gargiulo[4], Maryse Schmoetten[5], Laura Neises[1], Coralie Pulido[3], Nadia I. Lorenz[6-9], Michael W. Ronellenfitsch[6-9], David Sumpton[10], Marc Warmoes[11], Christian Jaeger[11], Antoine Lesur[1], Jerome Paggetti[4], Etienne Moussay[4], Simone P. Niclou[3], Elisabeth Letellier[5], Johannes Meiser[1]*

[1]Cancer Metabolism Group, Department of Cancer Research, Luxembourg Institute of Health, Luxembourg, Luxembourg;

[2]Faculty of Science, Technology and Medicine, University of Luxembourg, 2 avenue de Université, Esch-sur-Alzette, Luxembourg;

[3]NORLUX Neuro-Oncology Laboratory, Department of Cancer Research, Luxembourg Institute of Health, Luxembourg, Luxembourg;

[4]Tumor Stroma Interactions, Department of Cancer Research, Luxembourg Institute of Health, Luxembourg, Luxembourg;

[5]Molecular Disease Mechanisms Group, Faculty of Science, Technology and Medicine, Department of Life Sciences and Medicine, University of Luxembourg, Esch-sur-Alzette, Luxembourg;

[6]Dr. Senckenberg Institute of Neurooncology, University Hospital Frankfurt, Goethe University, Frankfurt am Main, Germany;

[7]German Cancer Consortium, Partner Site Frankfurt/Mainz, Frankfurt am Main, Germany;

[8]Frankfurt Cancer Institute (FCI), University Hospital Frankfurt, Goethe University, Frankfurt am Main, Germany;

[9]University Cancer Center Frankfurt (UCT), University Hospital Frankfurt, Goethe University, Frankfurt am Main, Germany;

[10]Cancer Research U.K. Beatson Institute, Switchback Rd, Bearsden, Glasgow G61 1BD, UK;

[11]Luxembourg Centre for Systems Biomedicine, University of Luxembourg, 6 Avenue du Swing, 4367 Esch-sur-Alzette, Luxembourg;

*Correspondence:

Email: johannes.meiser@lih.lu

Twitter: @JohannesMeiser

Abstract

Throughout the metastatic cascade, cancer cells are faced with harsh metabolic environments and nutritional stresses which apply selection pressure leaving only the most metabolically resilient cells to survive and form metastases. Metabolic characterisation of such cell populations *in vitro* is currently challenging. Using galactose as a tool compound to mimic glycolytic limitation within the tumour microenvironment of primary and secondary neoplastic sites, we were able to uncover metabolic flexibility and plasticity of cancer cells *in vitro*. In contrast to the established idea that high glycolytic flux and expression of PKM2 redirects carbons towards anabolic routes such as the pentose phosphate pathway and serine synthesis pathway (SSP), we have discovered by using stable-isotope tracing that also glycolytic limitation results in metabolic rewiring. Surprisingly, despite limited carbon availability and energetic stress, cells induce a near complete block of pyruvate kinase isozyme M2 (PKM2) to divert carbons towards SSP. Simultaneously, TCA cycle flux is sustained and oxygen consumption is increased, both supported by glutamine. Glutamine not only supports TCA cycle flux but also SSP via distinct mechanisms. Due to PKM2 block, malic enzyme exclusively supports TCA cycle flux while mitochondrial phosphoenolpyruvate carboxykinase supports SSP. Moreover, by using genetic modifications of different one-carbon (1C) cycle enzymes, we are able to reverse the PKM2 block suggesting a link between mitochondrial 1C cycle and pyruvate kinase. Thus we show that PKM2 inhibition acts as a branching point to direct glycolytic and glutamine carbons into distinct routes, overall supporting the metabolic plasticity and flexibility of cancer cells.

52

53 **Introduction**

54 Increased aerobic glycolysis has been identified as a characteristic of cancer cells almost 100 years ago and
55 subsequently highlighted as a hallmark of cancer [1-3]. This is the phenomenon whereby cancer cells increase
56 the fermentation of glucose to lactate even in the presence of oxygen, at the cost of releasing and thereby
57 losing carbons as lactate [4]. Many theories have been suggested as to why cancer cells adopt such a biomass-
58 wasteful and energy-inefficient phenotype with the majority of these theories circulating around the idea
59 that mitochondria is unable to cope with very high rates of early glycolytic reactions that support branched
60 biosynthetic pathways [5-7]. One reason cancer cells are committed to these early glycolytic steps is
61 oncogenic signalling [8-10]. In these early steps of glycolysis, ATP and NAD^+ are consumed and need to be
62 regenerated for glycolysis to continue. This regeneration of ATP and NAD^+ seems to be the decisive
63 bottleneck where the cancer cell has to decide whether to ferment glucose or oxidise it fully in the TCA cycle
64 [5, 11-13]. Indeed, two recent publications highlighted how aerobic glycolysis rates are decided based on
65 NADH shuttle capacity and the regeneration of NAD^+ [12, 13]. Moreover, it was proposed that cells
66 downregulate aerobic respiration to avoid ATP depletion when the mitochondria are unable to replenish ATP
67 used in the early steps of glycolysis fast enough. Therefore, cells turn to ATP generation via lactate overflow
68 to avoid an ATP crisis [4, 5, 11].

69 While it has been suggested that aerobic glycolysis is not the main driver of high proliferation rates [13], it
70 remains undeniable that cancer cells engage high proliferative rates in favourable metabolic environments
71 with ampleness of glucose being an example of such environments. However, glucose abundance will force
72 cancer cells into aerobic glycolysis for the reasons highlighted above. Therefore, *in vitro* it might seem that
73 cancer cells are fixed on aerobic glycolysis, while *in vivo* they display metabolic flexibility and plasticity [14].
74 Such metabolic malleability *in vivo* allows cancer cells to survive nutrient depleted and hostile metabolic
75 environments that arise within the tumour microenvironment (TME) due to poor vascularisation and high
76 proliferative rates. Moreover, cancer cells need to be metabolically flexible to survive the ever changing
77 metabolic environments throughout the metastatic cascade [15]. However, such metabolic flexibility is

usually masked within *in vitro* studies due to the usage of synthetic media which contain supraphysiological concentrations of several metabolites [16]. Aerobic glycolysis can be caused *in vitro* as cancer cells become reversibly addicted to glycolysis and repress their mitochondrial respiration in response to high glucose concentration in their respective media i.e. the Crabtree effect [11, 17].

One method to circumvent this glycolytic addiction *in vitro* to unmask cancer cells metabolic flexibility to study it, is to substitute glucose for galactose in culturing medium. Galactose is metabolised via the Leloir pathway to produce glucose 6-phosphate (G6P), meaning that it can support glycolysis [18]. However, glucose is converted into G6P via one enzymatic step catalysed by hexokinase (Km ~ 0.3 mM) [19, 20], while galactose requires four biochemical reactions to continuously supply the cell with G6P with the initial reaction alone having a Km value three times lower than hexokinase (galactokinase Km ~ 1 mM) [21]. This results in galactose providing a slower than glucose, yet continuous, supply of carbons, mimicking the TME where glucose is rapidly consumed but continuously being replenished via circulation [22, 23]. Therefore, we used galactose as an *in vitro* tool compound to mimic glycolytic limitation that occurs within the TME.

We have previously shown that cancer cells increase serine catabolism and formate overflow under glycolytic limitation even though biosynthetic demands were decreased [24], indicating a role for one-carbon (1C) cycle in bioenergetics and redox balance [25]. However, the functional advantage and the exact source of carbons for the increased serine catabolism and formate overflow under glycolytic limitation remains unanswered. Moreover, it was previously highlighted that glutamine flux is rewired towards serine synthesis pathway (SSP) under glucose starvation via phosphoenolpyruvate carboxykinase 2 (PEPCK2) [26-29]. Both observations indicate that metabolic rewiring takes place towards SSP under glycolytic limitation, yet the exact mechanisms and metabolic advantages of this rewiring remain unclear. Building on these observations, we used stable-isotopic tracers and targeted metabolomics to study the metabolic fluxes of central carbon metabolism and the rewiring that takes place under glycolytic limitation. By using galactose to model glycolytic limitation, we observed a continued but decreased flux through glycolysis while oxygen consumption rates (OCR) were increased [24]. We were able to corroborate previous findings on the rewiring of glutamine metabolism towards SSP via PEPCK2. Surprisingly and despite increased OCR, galactose derived

104 carbons did not enter the TCA cycle for mitochondrial oxidation, suggesting glutamine is the main substrate
105 to support the TCA cycle in these conditions. This block on glycolytic carbons toward mitochondrial
106 metabolism is facilitated by a strong pyruvate kinase isozyme M2 (PKM2) block, pinpointing PKM2 as the
107 rewiring point in glycolysis under glycolytic limitation. Furthermore, we observed that the PKM2 block
108 redirects the limited glycolytic carbons toward SSP to support the survival and proliferation of cancer cells.
109 Finally, we observed an upregulation of the mitochondrial enzymes of 1C cycle where they cooperate to
110 support biosynthesis, bioenergetics and redox balance under glycolytic limitation. These findings reveal that
111 1C cycle is needed for the proliferation of cancer cells when faced with limited glycolytic supply, and blocking
112 lower glycolysis at PKM2 contributes to keeping the 1C cycle running in these conditions.

113 **Results**

114 **Cancer cells metabolize galactose and utilize it to support early glycolysis**

115 To ascertain that cancer cells are able to metabolize galactose (Gal), we used a fully labelled [U-^{13}C] Gal tracer
116 and compared the relative flux through the Leloir pathway (Fig. 1A) and early glycolysis to the fluxes
117 measured when a [U-^{13}C] glucose (Glc) tracer is used (Fig. 1B). The relative flux to UDP-glucose and UDP-
118 galactose was comparable between Glc and Gal tracing and even higher in the case of glucose 1-phosphate
119 in Gal (Fig. 1C-E). When looking at the glycolytic intermediate fructose 1,6-bisphosphate (F 1,6-BP), the ^{13}C
120 labelling pattern was comparable between both tracers suggesting a similar flux of Glc and Gal (Fig. 1F).
121 Pentose phosphate pathway (PPP) is usually highly enriched with ^{13}C within the first minutes of [U-^{13}C] Glc
122 tracing [30]. Consequently, we saw high enrichments using [U-^{13}C] Gal tracing in early PPP intermediate 6-
123 phosphogluconate M+6 (Fig. 1G). However, the ^{13}C enrichment in ribose 5-phosphate (R5P) and
124 sedoheptulose 7-phosphate (S7P) showed multiple labelled isotopologues indicating higher shunting of
125 carbons between PPP, early glycolysis and gluconeogenesis in Gal conditions (Fig. 1H, I). Overall, these data
126 demonstrate that cancer cells are able to utilise Gal to fuel early glycolysis and PPP intermediates through
127 the Leloir pathway.

128 **Glutamine and lactate maintain an upregulated oxidative TCA cycle function under glycolytic limitation**

129 To test the validity of using Gal as a tool compound to mimic glycolytic limitation, we sought to first measure
130 the contribution of other carbon sources to the TCA cycle that might support the elevated mitochondrial
131 metabolism under Gal as characterized by increased oxygen consumption rates (OCR) [24] (Fig. S1A). It was
132 previously shown that glutamine anaplerosis into the TCA cycle is increased under full glucose starvation [29,
133 31]. To test if this is also the case upon limited glycolytic flux (compared to full starvation), we first measured
134 glutamine consumption and observed generally no striking change in the consumption in multiple cancer cell
135 lines under glycolytic limitation (Fig. 2A). Subsequently, we performed [U-^{13}C] glutamine tracing in MDA-MB-
136 468, 4T1 and B16-F10 cell lines in Glc and Gal. Upon Gal, we noted an increased relative flux from glutamine
137 into the TCA cycle metabolites in all three cell lines (Fig. 2B-D), indicating that while the absolute consumption
138 was not changed, the usage of glutamine flux is altered. Under Glc, we observed that glutamine enrichment
139 in the TCA cycle metabolites decreased as we move away from glutamine. In contrast, the enrichment
140 remains unchanged under Gal (Fig. 2B-D), indicating that the TCA cycle is running with strongly reduced
141 carbon input from glycolysis. Yet, acetyl-CoA input is required to sustain glutamine oxidation through the
142 TCA cycle, hinting towards malic enzyme (ME) activity to sustain pyruvate levels under glycolytic limitation.
143 ME decarboxylates malate into pyruvate and indeed, we observed a substantial M+3 labelling of pyruvate
144 and lactate from [U-^{13}C] glutamine under glycolytic limitation (Fig. 2E and S1B). ME involvement is further
145 supported by an increase in citrate M+6 isotopologue enrichment from glutamine under Gal which suggests
146 increased usage of glutamine derived acetyl-CoA for citrate (Fig. 2F-H). Additionally, when looking at the ratio
147 of M+3 pyruvate/M+4 malate (ME flux), we observe a significant increase under glycolytic limitation (Fig. 2I)
148 [31]. These findings display the metabolic plasticity of cancer cells, as they are able to rewire their metabolism
149 to run the TCA cycle mainly on glutamine. However, we are still able to detect an unlabelled fraction in citrate
150 (Fig. 2F-H) which most likely results from fatty acid oxidation. An additional carbon source that we might
151 neglect with our *in vitro* setup is lactate whose build up is a prominent feature of most solid tumours [32]. In
152 fact, recent evidence from *in vivo* studies suggests that lactate can be a major carbon source to the TCA cycle
153 of cancer cells [33, 34]. To test if this feature can be recapitulated in our *in vitro* model, we performed [U-
154 ^{13}C] lactate tracing at a concentration of 5 mM as this was indicated as a physiological relevant concentration

155 within the TME [22, 35]. Supported by the increase in NAD^+/NADH ratio (Fig. 2J), we measured increased ^{13}C
156 contribution to pyruvate and the TCA cycle under glycolytic limitation (Fig. 2K, 2L and S1C, S1D). Of note, the
157 lactate derived carbon contribution to the TCA cycle was mainly via PDH and not via pyruvate carboxylase
158 (Fig S1E, S1F). In summary, we conclude that glutamine and lactate can substitute for glucose to support and
159 run lower glycolysis and the TCA cycle. In the case of lactate, this is facilitated by the increased NAD^+/NADH
160 ratio favouring lactate oxidation. Other carbon sources might also contribute towards the TCA cycle,
161 however, these contributions are expected to be smaller in comparison to the sources highlighted in this
162 study [33]. Finally, the sustained PDH flux under Gal suggests that a block upstream of PDH prevents glycolysis
163 derived entry into the TCA cycle (Fig. 2B-D).

164 **Glutamine metabolism is redirected towards SSP under glycolytic limitation via PEPCK2**

165 It has previously been shown that under full glucose starvation, gluconeogenesis enzyme PEPCK2 becomes
166 active and supports the biosynthesis of glycolytic intermediates [26-29, 36]. To test if this also the case in Gal
167 and not only upon full hexose starvation, we monitored glutamine derived carbon contribution to
168 phosphoenolpyruvate (PEP) and 3-PG (Fig. S2A-B) and observed an active PEPCK flux also upon low glycolytic
169 flux. Furthermore, we observed that the ^{13}C enrichment was further increased under serine/glycine (SG)
170 starvation conditions. Overall, we were able to confirm PEPCK activity in three different cancer cell lines with
171 up to 30% of the measured serine being fully labelled under SG starvation (Fig. 3A). Even with SG in the
172 medium, the glutamine flux to serine was comparable to the one from Glc (Fig. 3B). As serine is the major
173 substrate for 1C metabolism, we measured the flux from glutamine into vital downstream metabolites of 1C
174 metabolism. We observed ^{13}C enrichment in ATP (Fig. 3C), glutathione (GSH) (Fig. 3D) and formate (Fig. S2C).
175 Of note, the labelled fraction of ATP reached an astonishing 40-50% under SG starvation in all three cell lines
176 (Fig. 3C).

177 PEPCK catalyses the decarboxylation of oxaloacetate into PEP, therefore, we can measure its metabolic flux
178 by using aspartate as a surrogate for oxaloacetate as the tracer medium contains no aspartate [37]. Doing
179 so, we observed a clear increase in PEPCK flux under glycolytic limitation with and without SG (Fig. 3E).
180 Mitochondrial PEPCK (PEPCK2) has been identified as the major isoform present in most tumour tissues [26].

181 Here we observed that PEPCK2 protein expression was markedly increased under glycolytic limitation in all
182 the cell lines tested (Fig. S2D). Subsequently, we used two different genetic approaches to target PEPCK2;
183 we knocked down PEPCK2 in MDA-MB-468 cells using shRNA and knocked it out using CRISPR/Cas9 system
184 in 4T1 and B16-F10 cells (Fig. S2E, F). Overall, we were able to confirm PEPCK2 as the culprit for the ^{13}C
185 enrichment into serine from glutamine (Fig. 3F). More importantly, serine intracellular levels significantly
186 dropped in MDA-MB-468 and 4T1 but not in B16-F10, signifying the importance of the glutamine flux for the
187 serine pool while also highlighting varying cell line specific dependencies on PEPCK2 (Fig. 3G). Furthermore,
188 the labelling into ATP and GSH was significantly reduced in PCK2 KD and eliminated in the KOs (Fig. 3H, I) and
189 formate overflow was mildly decreased in the PCK2 KOs (Fig. S2G). Moreover, we observed a mild increase
190 in the labelling of TCA cycle intermediates and pyruvate from glutamine in PCK2 KD/KOs which most likely is
191 a result of the elimination of the flux through PEPCK (Fig. S2H, I). Despite the significance of the glutamine
192 flux into SSP we noted no difference in proliferation of 4T1 PCK2KO under glycolytic limitation (Fig. 3J). This
193 indicates that 4T1 cells are able to compensate for the missing contribution into serine by either increasing
194 uptake of serine from the medium or increasing the flux from Gal under SG starvation (Fig. S2J). Overall, by
195 using Gal as a tool compound, we were able to see that glutamine metabolism is rewired in cancer cells to
196 run the TCA cycle solely and to support SSP via enhanced activity of PEPCK2 (Fig. 3K). However, it remains
197 unclear how PEPCK2 and ME fluxes are coordinated as these fluxes cannot be disentangled by using [U-^{13}C]
198 glutamine. Therefore, we opted to use [U-^{13}C] Gal as a tracer to clearly follow the glycolytic flux into lower
199 glycolysis and TCA cycle under glycolytic limitation.

200 **Cancer cells sustain carbon flux towards SSP under glycolytic limitation**

201 To study the relative fluxes of lower glycolysis under glycolytic limitation in more detail we used [U-^{13}C] Gal.
202 Across a panel of nine different cancer cell lines representing four different tumours (breast, colorectal,
203 glioblastoma and melanoma) we observed robust Gal metabolization through glycolysis (Fig. 4A-C). Despite
204 similar enrichment in F 1,6-BP (Fig. 1F), the relative flux of ^{13}C in Gal decreased towards late glycolytic
205 intermediates especially pyruvate with ^{13}C enrichment of about 10% compared to the flux under Glc (Fig. 4B).
206 In comparison, cells appeared to keep about 25 – 50% of their relative flux towards serine under Gal (Fig.

207 4C). To exclude that this effect is due to differences in the time needed to reach isotopic steady state [37],
208 we performed a time course experiment. We observed isotopic steady state conditions with both tracers at
209 around 24h and longer incubation times did not result in higher ^{13}C enrichment of pyruvate, suggesting that
210 the different labelling pattern in pyruvate is not a result of different flux rates but of an alteration of central
211 carbon metabolism upon Gal (Fig. S3A). Furthermore, different Gal concentrations also did not affect how
212 much [U-^{13}C] Gal enriched the pyruvate pool (Fig. S3A). Using dialysed or normal FBS did not affect pyruvate
213 enrichment as well (Fig. S3B). To eliminate the possibility of an inhibitory action of Gal, we mixed Glc and Gal
214 in a 1:1 mix where the Glc added was ^{13}C. If Gal had a direct inhibitory action on glycolysis we would expect
215 to see a clear reduction of ^{13}C flux towards pyruvate, however, we observed no difference in ^{13}C enrichment
216 in glycolysis under such conditions (Fig. S3C). These observations indicate that the reduced glycolytic ^{13}C flux
217 is a result of the cells' response to the limited availability of Gal carbons.
218 To better visualise the differences between the relative flux towards lower glycolysis and SSP, we used 3-PG
219 (divergent point between SSP and lower glycolysis) M+3 isotopologue as a common denominator to
220 normalise the main labelled isotopologue of different metabolites (e.g. M+3 serine/M+3 3PG, M+3
221 pyruvate/M+3 3PG, M+2 citrate/M+3 3PG etc). These ratios are presented as a fold change of the same
222 ratios under Glc (Fig. 4D, E). We found that in most cell lines the ratio for serine under Gal was comparable
223 or higher than under Glc, which indicates comparable or higher flux to SSP under glycolytic limitation. In
224 contrast, the ratio of M+3 pyruvate / M+3 3PG was strikingly lower under Gal than under Glc, which indicates
225 significantly less carbon flux towards pyruvate under Gal. Thus, we observed that cancer cells re-wire their
226 limited ^{13}C supply under Gal towards SSP resulting in SSP as the significantly more favoured destination than
227 lower glycolysis. This phenotype was predominant in cell lines which doubled under 24h (fast-growing) (Fig.
228 4D, E). One exception was the murine breast cancer cell line 4T1, which is extremely glycolytic and is very
229 sensitive to galactose, indicating that this cell line may not be able to adapt to such an environment (Fig. 4E).
230 Furthermore, we took note of a similar observation of the rewiring when looking at the intracellular levels of
231 serine and pyruvate (Fig. 4F, G). When looking at the ^{13}C flux ratios when ^{13}C-Glc is mixed 1:1 with ^{12}C-Gal we
232 saw that there was no change in the ratios, showing again that Gal is not inhibitory of glycolysis (Fig. 4H).

233 However, when ^{13}C-Gal was mixed with ^{12}C-Glc we saw that the flux was heavily favoured towards pyruvate
234 and lactate and not to SSP (Fig. 4H). Such observation indicate that under ample supply of glycolytic carbons,
235 ^{13}C flux from Gal is not rewired towards SSP.
236 Based on the observed rewiring, we checked the expression of SSP enzymes and observed a modest increase
237 in the protein expression of phosphoserine aminotransferase 1 (PSAT1) and phosphoserine phosphatase
238 (PSPH), while phosphoglycerate dehydrogenase (PHGDH) expression was mostly not elevated (Fig. S3D, S3E).
239 This indicates that the sustained flux through SSP is not a result of altered gene expression but rather a more
240 direct metabolic adaptation of enzyme activity. In summary, under glycolytic limitation, fast-growing cancer
241 cells (cell lines with doubling times <24 hours) re-wire their metabolism upon limited glycolytic flux towards
242 SSP at the cost of pyruvate oxidation.
243 **Glycolytic limitation inhibits glycolysis at PKM2**
244 Having identified a block at lower glycolysis and re-routing of glycolytic carbos towards SSP, we looked to
245 determine how cancer cells mechanistically undergo the proposed re-wiring. Since the re-wiring happens
246 somewhere between 3-PG and pyruvate, we hypothesised that this might occur at pyruvate kinase which is
247 a known regulatory node of glycolysis [38] (Fig. 5A). This hypothesis is supported by the observation that
248 under Gal cancer cells excrete almost no lactate (Fig. S4A) and its intracellular levels drop significantly (Fig.
249 4F). This finding also explains why cancer cells are very vulnerable to adenine nucleotide translocator (ANT)
250 inhibition under glucose starvation [39] as in the absence of lactate production they would be highly relying
251 on mitochondrial ATP. Specifically, we have observed that PEP accumulates under Gal while pyruvate levels
252 drop dramatically (Fig. 5B-E), further supporting the hypothesis that the metabolic block occurs at the level
253 of PKM. This is further substantiated by the observation that ^{13}C labelling in pyruvate is nearly absent across
254 all cell lines analyzed, while PEP remains significantly labelled (Fig. 5B-E). To confirm the glycolytic block at
255 PKM2, we used the PKM2 activator TEPP-46 [40] and repeated stable isotope tracing with [U-^{13}C] Gal. The
256 activation of PKM2 increased the ^{13}C flux towards citrate at the cost of serine (Fig. 5F). Furthermore, we
257 observed a significant reduction of the labelling into serine using [U-^{13}C] glutamine solidifying our model that
258 the rewiring into SSP is supported by PKM2 inhibition (Fig. S4B). Finally, the activation of PKM2 and

subsequent prevention of the rewiring towards SSP lead to a significant decrease in proliferation of MDA-MB-468 (Fig. 5G), concluding that maybe not the PEPCK2 flux but the PKM2 flux is important for survival, at least in our experimental setup (Fig. 3J, 5G).

In summary, we provide so far evidence that when hexose availability for glycolysis is limited, the residual glycolytic carbon remains in upper glycolysis to support SSP. Meanwhile, glutamine and lactate compensate for carbon demand of the TCA cycle to support increased mitochondrial respiration. Moreover, we are able to increase the mechanistic granularity of the glutamine rewiring through ME and PEPCK by identifying the PKM2 block which means that ME flux (Gln --> Pyruvate) is exclusive to supporting the TCA cycle while PEPCK flux (Gln --> PEP) is exclusive to support SSP (Fig. 5H).

SSP is needed for proliferation and viability under glycolytic limitation

Next, we sought to investigate the functional advantage of the observed metabolic re-wiring towards SSP. We noted a weak correlation between the growth rate of cancer cells and how much Gal inhibited their proliferation (Fig. 6A). Based on that observation we studied the proliferative potential of the MDA-MB-468 cell line when treated with a competitive inhibitor of PHGDH (the rate-limiting enzyme of SSP) BI-4916 [41] while under glycolytic limitation. We observed the lowest proliferative capacity of MDA-MB-468 cells when SSP was inhibited under glycolytic limitation (Fig. 6B). We further validated our results when MDA-MB-468 cells were grown in 3D using anchorage independent conditions with both normal and dialysed FBS (Fig. 6C, D and S5A). We confirmed these observations by repeating our proliferation assay in different cancer cell lines while obtaining similar results in 2 out of the 3 cell lines tested (Fig. 6E). Lastly, we looked at the viability of different cancer cells when cultured in Gal and treated with BI-4916. We saw increased percentage of apoptotic (Ann V^+) cells when PHGDH flux is blocked under glycolytic limitation (Fig. 6F), with the exception again of 4T1 cells which matches the fact they were the only cell line not showcasing the observed rewiring towards SSP (Fig. 4E). Overall, it is evident that SSP supports proliferation under glycolytic limitation.

SSP flux is crucial to sustain mitochondrial formate production and to support all three metabolic pillars

In addition to serine synthesis, we were interested to understand functional relevance of sustained serine availability. We sought to uncover the metabolic purpose of such rewiring, especially since 1C metabolism is able to support all of the three metabolic pillars; biosynthesis, bioenergetics and redox balance [25] (Fig. 7A). We looked into the expression of the different enzymes of the 1C cycle and noticed that the mitochondrial enzymes SHMT2 and MTHFD2 had increased expression under glycolytic limitation while their cytoplasmic versions were unchanged (Fig. 7B-C). The product of the mitochondrial 1C cycle branch is the release of the 1C unit as formate and we have previously shown that serine catabolism and formate overflow increase upon Gal [24]. In corroboration, we performed formate measurements in the same panel of cancer cell lines used in Figure 4 and observed increased formate release under glycolytic limitation in all the cell lines tested (Fig. 7D). Similar to lactate overflow, formate overflow produces one ATP per reaction. In addition to ATP production, formate overflow can yield 1 NADH molecule via MTHFD2 [42]. The coupling of MTHFD2-derived NADH to electron transport chain (ETC) thereby contribute to mitochondrial ATP production and the observed increase in OCR (Fig. S1A)[24]. Meaning that the increased formate release can serve a crucial bioenergetic function under glycolytic limitation [24]. Furthermore, we have previously shown that under glycolytic limitation, AMPK is activated alongside the increased formate release [24]. To test whether AMPK is responsible for the rewiring towards SSP and 1C cycle, we utilized LN-229 glioblastoma cell line harbouring a genetic deletion of both alpha subunits of AMPK[43]. We observed no difference in the AMPK KO cells in terms of formate release (Fig. S6A) and ^{13}C flux rewiring (Fig. S6B), indicating that AMPK activation and increased formate overflow are not in causal relation. Knocking-out MTHFD1L (enzyme catalysing formate release) in MDA-MB-468 cells led to only a subtle decrease in growth in 3D anchorage-independent conditions under glycolytic limitation (Fig. S6C, D).

Having observed that bioenergetic aspect might only partially contribute to the functional implications during glycolytic restriction, we investigated potential additional derived metabolic aspects of the 1C cycle that support redox balance and biosynthesis. The 1C unit donated by serine can either be used for de novo purine and pyrimidine synthesis or oxidised to CO_2 via ALDH1L2 or ALDH1L1 while generating NADPH in the latter process (Fig. 7A). NADPH provides the cell with reducing equivalents required to counter reactive oxygen

309 species (ROS). We explored both biosynthesis and redox balance as potential sinks for the rewired ^{13}C flux.
310 ALDH1L2 expression was markedly increased under glycolytic limitations in different cancer cell lines while
311 the expression of ALDH1L1 was unchanged (Fig. 7B, 7E). Indicating that 1C metabolism is mostly involved in
312 maintaining mitochondrial rather than cytosolic redox state under glycolytic limitation. Moreover, when we
313 grew the highly glycolytic breast cancer cell line 4T1 (Fig. S4A) for 72h in Glc without medium change, we saw
314 that the expression of ALDH1L2 increased as Glc concentration became limited supporting the data we
315 obtained using Gal (Fig. 7G). Knocking out ALDH1L2 (Fig. S6E) resulted in mildly reduced proliferation under
316 glycolytic limitation in both 2D and 3D assays (Fig. 7H, I). Increased expression of ALDH1L2 and increased
317 formate overflow at the same time would together highlight the increase of the carbon flux through SSP and
318 1C cycle as despite the release of 1C as CO_2, formate overflow is still significantly increased.
319 PPP is a key regulator of biosynthesis and redox balance as it supplies the cells with R5P and NADPH [44]. The
320 cycling of carbons we observed in Fig. 1H, I suggests that PPP is shifted towards maximising the production
321 of NADPH and R5P from the limited carbon supply. Due to the carbon cycling in PPP, it is not possible to
322 determine the contribution of 1C metabolism towards nucleotide biosynthesis using [U-^{13}C] Glc and Gal
323 tracers (Fig 7J and S6F-J). Therefore, we utilised [U-^{13}C] serine tracer and observed that the flux from serine
324 towards nucleotide biosynthesis is maintained under glycolytic limitation (Fig. 7K). Overall, it can be
325 concluded that the individual metabolic functions of the 1C metabolism are only partially contributing to the
326 functionality of cells under glycolytic limitation. Conclusively, this suggests the idea that the flux through the
327 mitochondrial 1C cycle might serve multiple metabolic purposes.
328 To test if mitochondrial 1C metabolism plays a role in controlling metabolic adaptation at glycolytic limitation
329 we performed [U-^{13}C] Gal tracing in MTHFD1L and MTHFD2 KOs (Fig. S6E) and found that the ^{13}C flux rewiring
330 towards SSP is decreased (decrease in ^{13}C to serine and glycine and increase to citrate) (Fig. 7L, M). These
331 observations indicate that the mitochondrial 1C pathway is a meaningful factor responsible for the rewiring
332 of lower glycolysis.
333 Put together, it is apparent that the rewiring towards SSP and plasticity of 1C metabolism under glycolytic
334 limitation serves all three metabolic pillars with sustained carbon flux from serine to purines and increased

ATP and NADPH generation. In particular, mitochondrial formate production needs to be increased, as an increased fraction of formate is likely to be oxidized via ALDH1L2 while at the same time formate overflow is also increased. Additionally, cytosolic formate is needed to support purine and pyrimidine biosynthesis to sustain proliferation.

***In vivo* relevance of using Gal to model glycolytic limitation**

Modelling the metabolic environment that cancer cells face *in vivo* is extremely challenging due to the heterogeneity of the tumour and the varying metabolite composition of the TME. Using Gal as a tool we have aimed to mimic one important variable of the *in vivo* TME: glucose limitation. To test the physiological relevance of using Gal as a tool compound to study glycolytic limitation, we subcutaneously injected B16-F10 cells in the flanks of C57BL/6 mice, allowed the tumours to grow for X and Y days (thereby generating larger and smaller tumours) (Fig. 8A) and then we infused the mice under anaesthesia with [U-^{13}C] Glc tracer for 2 hours. Next, we performed targeted metabolomics on pieces of dissected tumour and compared the small tumours to the inside and the outside of the big tumours to primarily measure the gradient of metabolite levels between the outer layer and the core of the relatively big tumours. We observed that glucose levels drop in the core compared to the outer layer, while other metabolites that can act as secondary carbon sources for tumours (lactate, glutamine and serine) were all present at similar levels between the two layers (Fig. 8B). Moreover, when looking at the MIDs of 3-PG we can see that the ^{13}C enrichment is slightly higher on the outer layer (Fig. 8C). *In vivo*, when the ^{13}C fraction of pyruvate is normalised to the ^{13}C fraction of 3-PG, the result is 1 when newly synthesised pyruvate is entirely generated by glycolysis and >1 when other ^{13}C sources outside of glycolysis (labelled elsewhere by U-^{13}C Glc and supply the tumour from circulation) contribute to the pyruvate pool [34]. Comparing these ratios between the outer and inner layers of the B16-F10 tumours, we can see that the ratio is ~ 2.3 in the inner core and 1.5 in the outer layer (Fig. 8D). This indicates that tumours are depleted of glucose in bigger tumours and are relying more on other carbon sources in these instances due to altering their glycolytic usage i.e. metabolic flexibility. In contrast, serine ratios remain rather constant suggesting a switch of the glycolytic flux towards serine (Fig. 8D).

A further *in vivo* model we utilised is the adoptive transfer of TCL1-355 into C57BL/6 mice as a model of chronic lymphocytic leukaemia (CLL) [45, 46]. In this model, leukemic B cells proliferate rapidly within the spleen which in theory should create areas depleted of glucose as within solid tumours which is what we are mimicking *in vitro* using Gal. Indeed, we have observed decreased glucose concentration in the spleens of CLL mice compared to healthy mice (Fig. 8E). After the disease developed, mice were continuously infused via the tail vein with [U-^{13}C] Glc tracer for 2 hours. Comparing B cells from healthy spleens against CLL B cells from diseased spleens, we observed that CLL cells significantly increased their relative flux from glucose towards serine and glycine while having a reduced flux towards citrate, indicating low pyruvate oxidation (Fig. 8F). This altered metabolic phenotype between normal and leukemic B cells *in vivo* is partly recapitulated *in vitro* by switching cancer cells from Glc to Gal. In summary, by using Gal we are able to capture relevant metabolic features of tumour cells that occur in glucose depleted TME, specifically, the glycolytic rewiring towards serine to support cancer cell metabolism.

Discussion

In the present study, we discover a novel rewiring of glycolytic flux towards SSP via a PKM2 block when the supply of glycolytic carbons is inadequate as modelled with Gal as a tool compound to mimic glycolytic limitation within the TME. In addition, we were able to corroborate previously described rewiring of glutamine metabolism towards SSP, however, by identifying the PKM2 block, we were able to deepen our understanding of this rewiring to differentiate the glutamine flux under glycolytic limitation to either exclusively support SSP or TCA cycle via PEPCK2 or ME, respectively (Fig. 5H). We observed that both fluxes contribute to the survival and proliferation of several cancer cell lines and to supply the 1C cycle with the necessary carbons to perform biosynthetic, bioenergetic and redox balance functions.

Cancer cells *in vitro* usually engage in aerobic glycolysis due to the ample availability of glucose which does not reflect what occurs within the TME. A key metabolite that drives the metabolic phenotype of cancer cells is glucose and its availability, which has been shown to be decreased in the tumour interstitial fluid (TIF) when compared to plasma [22, 23]. TIF measurements represent the average level of glucose across the area of the tumour. However, inside the tumour, areas do exist where cells are even more deprived of glucose

386 (Fig. 8B) and those cells withstanding such severe metabolic stress (alongside other niche stresses) are the
387 plastic cells that are capable of surviving the metastatic cascade [15]. Uncovering the metabolic rewiring in
388 these deprived cells hold therapeutic promise to target cancer growth and metastasis [25].
389 By culturing cancer cells under glycolytic stress, we are able to see their ability to use the same carbon source
390 for different functions (metabolic plasticity) with the PKM2 block and rewiring of carbons towards SSP. On
391 the other hand, cancer cells also re-direct the glutamine flux towards SSP showcasing an example of
392 metabolic flexibility [14]. PEPCK2 is the main instigator of glutamine flux rewiring towards SSP. It is intriguing
393 that the mitochondrial isoform of PEPCK is involved under glycolytic limitations, as usually this isoform is only
394 involved when cytoplasmic NADH levels are not depleted. However, under glycolytic limitations, NAD/NADH
395 ratio is increased and yet the cells preferably engages PEPCK2 over cytoplasmic PEPCK1 (PEPCK1 involvement
396 would transfer mitochondrial NADH to the cytoplasm via malate oxidation). This can be explained by the
397 possibility that the gluconeogenesis pathway is activated mainly to support SSP and therefore, cytoplasmic
398 NADH is not required to reduce 1,3-bisphosphoglycerate into glyceraldehyde 3-phosphate. Furthermore, in
399 our system we did not observe a proliferative advantage in activating PEPCK2 under glycolytic limitation
400 contrary to what has previously been published on PEPCK2. One major difference in our setup that could
401 explain this observation is the usage of cell lines which have PHGDH amplification and are capable of
402 increasing their serine synthesis flux.
403 The diversion of the glycolytic flux away from lower glycolysis (3-PG onwards) and towards SSP offers many
404 metabolic advantages for the cell. For bioenergetics, SSP and subsequent 1C cycle generate two NADH and
405 one ATP per 3-PG molecule, while lower glycolysis generates one ATP and consumes one NADH. Meaning
406 that if energy is the main constraint for the cell under glycolytic limitation, it will benefit more from running
407 SSP and the subsequent serine catabolism and formate overflow [24]. Furthermore, the advantage of
408 maintaining the flux towards serine catabolism, lies in its flexibility. The fate of the 1C can be tailored for the
409 cell's need; fully oxidising it via ALDH1L2 will generate NADPH, MTHFD1L reaction will generate ATP, or it can
410 be incorporated in purines and dTMP in the cytosol [25]. Here we show that under glycolytic limitation, the
411 rewiring towards SSP and 1C cycle support all the three different pillars of metabolism, specifically the

412 mitochondrial part of the 1C cycle (Fig. 4). In fact, we observe that even though the cells increase the
413 expression of ALDH1L2 and subsequently lose more carbon as CO_2, formate overflow is still increased,
414 highlighting the non-biosynthetic benefit of running the mitochondrial branch of the 1C cycle under glycolytic
415 limitation.

416 Previous work have shown that serine acts as an allosteric activator of PKM2, while the lack of extracellular
417 serine lead to an inhibition of PKM2 activity [47, 48]. Here we observed that when glucose is limited, even
418 with serine/glycine available in the media, PKM glycolytic flux was inhibited. Indicating that even when serine
419 was available for the cells, the lack of glycolytic carbons inhibited pyruvate kinase activity to rewire the flux
420 towards SSP. This observation highlights an intriguing difference between de novo serine synthesis flux and
421 extracellular serine and potentially could be explained by recent work that has shown that PHGDH functions
422 beyond its catalytic activity within tumour cells and can allosterically regulate the function of
423 phosphofructokinase [49]. Moreover, here we presented evidence that the removal of MTHFD2 or MTHFD1L
424 was enough to re-establish PKM2 activity, meaning that mitochondrial 1C cycle is able to regulate PKM2
425 function. This would hint at a possible link between the PKM2 block and the increased formate overflow
426 under glycolytic limitation. Entangling the direct cause of PKM2 block and the link with 1C cycle is the subject
427 of ongoing work in our lab.

428 The findings presented here highlight the flexibility and plasticity of the biochemical network in tumour cells.
429 These traits present a challenge in developing precision-medicine drugs that target the cells' metabolism. For
430 such therapeutic strategies to be successful, context dependent understanding of environment conditions
431 and nutrient availability of the TME need to be considered alongside specific driver mutations [50].

432 **Acknowledgements:**

433 We are grateful to Stephanie Kreis (University of Luxembourg) for providing us with B16-F10, A375, SKMeL28
434 cells, Clement Thomas (LIH, Luxembourg) for providing 4T1 and BT-20 cells and Lewis Cantley (Harvard
435 Medical School) for providing MDA-MB-468 WT and MTHFD1LKO cells. We are grateful for all the technical
436 and analytical support from the different metabolomics platforms towards the work presented here and in
437 specific: Francois Bernardin from the metabolomics platform at LIH, Xiangyi Dong, Floriane Gavotto and Lucia

Gallucci from the LCSB metabolomics platform, Luxembourg. We are thankful for the support of the National Cytometry Platform (Quantitative Biology Unit, LIH) for support with flow cytometry measurements and analysis. Figures 1A, 1B, 3K, 5A, 5H and 7A were created with biorender.com.

M.B. is supported by the Fondation du Pélican de Mie et Pierre Hippert-Faber, under the aegis of the Fondation de Luxembourg. M.B. and J.M. are supported by the FNR-ATTRACT program (A18/BM/11809970). J.M. is supported by FNR-PRIDE NEXTIMMUNE (PRIDE/11012546), FNR-PRIDE i2Tron (PRIDE19/14254520). E.L. is supported by the FNR-CORE program (C16/BM/11282028 and C20/BM/14591557), by a Proof of Concept FNR grant (PoC/18/12554295), a PRIDE17/11823097 and by i2Tron (PRIDE19/14254520). E.G., J.P., and E.M. are supported by FNR programs: (PRIDE15/10675146/CANBIO, C20/BM/14582635, and C20/BM/14592342). E.V. is supported by FNRS-Télévie (7.4509.20 and 7.4572.22).

Material and Methods:

Chemicals

Galactose, glucose, serine, glutamine and glycine were purchased from Sigma Aldrich and stock solutions were prepared in ^{MQ}water. BI-4916 and TEPP-46 were purchased from MedChemExpress and stocks were prepared in DMSO. BI-4916 was always used at a final concentration of 15µM while TEPP-46 was used at 100µM.

Cell culture

MDA-MB468, 4T1, MDA-MB-231, HCT116, LN-229 and B16-F10 were cultured in DMEM (Thermo Fisher Scientific, 1443001) supplemented with 17.5 mM glucose, 2mM glutamine and 10% FBS. BT20 were cultured in advanced DMEM/F12 (Thermo Fisher Scientific, 12634010) supplemented with 2 mM glutamine and 10%FBS. A375 and SKMeL28 were cultured in RPMI 1640 (Thermo Fisher Scientific, 61870010) supplemented with 10%FBS. All cells were maintained at 37°C and 5% CO_2 and routinely tested for mycoplasma contamination. Serine/glycine starvation experiments were carried out using customised DMEM without phenol red, glucose, serine, glycine, tryptophan, pyruvate and glutamine with the missing ingredients added according to the concentrations present in full DMEM and experimental setup (Thermo Fisher Scientific). All experiments (except anchorage independent growth assays, see below) were seeded on D-1 and cells were allowed to adhere and attach overnight. Medium was aspirated and experimental medium plus treatment was added for the indicated time points in figures.

MDA-MB-468 WT and MTHFD1L-KO were received from Lewis Cantley lab, Weill Cornell Medical College, USA [51]. STR profiling in our lab in 2021 authenticated MDA-MB-468. LN-229 WT and AMPK-dKO cells were obtained from Michael Ronellenfitsch, Dr Senckenberg Institute of Neurooncology, University Hospital

Frankfurt, Goethe University and have been previously described in [43], B16-F10, A375 and SKMeL28 cells were received from Stephanie Kreis lab, University of Luxembourg, Luxembourg. 4T1 and BT20 were received from Clement Thomas lab, Luxembourg institute of Health, Luxembourg. MDA-MB-231 were obtained from Alexei Vasquez lab, Beatson Institute of Cancer Research, UK. All cell lines were originally purchased from ATCC.

Lentiviral mediated knockdown of *PCK2*

The procedure followed was described in detail in[52]. For silencing *PCK2* gene in MDA-MB-468 cells, pGIPZ shPCK2-2: ATTATTGGACAGTCTTTGT (V3LHS_410309) vector plasmid purchased from Horizon Discovery was used.

CRISPR/Cas9 KO of *Pck2, MTHFD2, ALDH1L2*

MDA-MB-468 cells harbouring deletion of MTHFD2 and ALHD1L2 have been previously generated in [52]. To KO *Pck2* in 4T1 and B16-F10, we used the same procedure described in [52]; two different gRNAs were used: 1. TATGCGTATTATGACCCGCC (Vector ID: VB211125-1122kdb, gRNA #654) to generate 4T1 clone A9 and B16-F10 clone A5. 2. GCGGGTCATAATACGCATAC (Vector ID: VB211125-1123gfv, gRNA #653) to generate 4T1 clone B7 and B16-F10 clone A9.

Animal experiments

All experiments involving laboratory animals were conducted in a specific pathogen-free animal facility with the approval of the animal welfare structure of LIH and the Luxembourg Ministry for Agriculture, Viticulture and rural development under the references LUPA 2021/08 and LUPA 2021/22. Mice were treated in accordance with the European Directive 2010/63/EU. C57BL/6 mice were purchased from Janviers Labs (France).

TCL1-355 adoptive transfer

The TCL1-355 murine cell line was kindly provided by Dr Efremov [46]. A total of 2,000 TCL1-355 cells resuspended in DMEM without phenol red were injected intravenously (iv; 100 µL) in the tail vein of C57BL/6 mice. CLL progression was monitored by determining the percentage of $CD5^{+}CD19^{+}$ circulating CLL cells in the peripheral blood. 14 days after iv injection, leukemic mice and age matched control mice were anaesthetised with 2.0 – 2.5 % of isoflurane and continuously infused with [U-^{13}C] glucose (50 % solution in 0.9 % NaCl) for 2h at a constant rate of 1.8g/Kg/h via the tail vein. At the end of the infusion, mice were euthanized via cervical dislocation and blood, organs and cells collection was rapidly performed.

Retro orbital blood sampling was performed before and after infusion. Plasma was collected after two successive centrifugations at 1000 RCF for 10 min. B cells were isolated from the spleen. Briefly, suspension of splenocytes was prepared using gentleMACS™ Dissociator (Miltenyi). Then, B cells isolation (negative sorting) was performed using MojoSort™ Mouse Pan B Cell Isolation Kit II (Miltenyi), according to

manufacturer's instructions. Cells were counted prior to pelleting and snap freezing. Pieces of spleen were also snap frozen in liquid nitrogen for metabolomics.

B16-F10 subcutaneous model

A total of 250,000 B16-F10 cells resuspended in PBS were injected subcutaneously (100 µL) into the flank of C57BL/6 mice and tumours were allowed to grow for 16 days for one group and 9 days for the second group. At endpoint, both groups were infused with [U-^{13}C] glucose as described above. After infusion, mice were euthanized with cervical dislocation and blood was collected into heparin tubes to separate plasma and tumour tissue was snap frozen in liquid nitrogen.

Western blot

KOs and KDs cell pellets were directly obtained from cell culture by pelleting cells at 350 RCF for 5 min followed by a PBS wash and then freezing at -20°C awaiting cell lysis. Probing protein expression after treatments: cells were cultured at 150,000 cells/well density in a 6-well plate on D-1. At time point of extraction, the plate was placed on ice, medium was aspirated and cells were washed in ice-cold PBS. Cell lysis buffer (150 mM NaCl, 1 mM EDTA, 50 mM Tris-HCl, 1% NP-40 with proteases and phosphatases inhibitors (Roche)) was added directly to the wells and cells were scraped and collected in pre-cooled Eppendorf tubes followed by sonification for 10 min. Lysates were spun at 16,000 RCF, 4°C for 10 minutes, the supernatant was collected in new tubes and the concentration of protein was determined with a Bradford assay. 20 – 40 µg of total protein was loaded into 15-well or 12-well RunBlue 4-12% Bis-Tris gels (Westburg) with the addition of 10mM DTT (Sigma Aldrich) and 4x NuPage LDS Sample buffer (Thermo Fisher Scientific) and gels were run for 90 minutes at 120V. Protein bands were blotted onto nitrocellulose membrane for 2h at 30 V. Membranes were blocked using 5 % milk powder in TBS-0.1 % Tween solution for 1h at RT. Membranes were incubated in the corresponding primary antibody overnight at 4°C and for 1h at RT in secondary antibodies. Detection of protein bands was done using Odyssey CLx Infrared Imaging system (LI-COR). Image StudioLite software Vers.5.2 (LI-COR) was used for quantifications and analysis. Primary antibodies used in this paper: MTHFD2 (Cell Signalling Technology, 41377), ALHD1L2 (Sigma Aldrich, HPA020549), β-Actin (Cell Signalling Technology, 3700), PSAT1 (Sigma Aldrich, HPA042924), PSPH (Sigma Aldrich, HPA020376), PHGDH (Sigma Aldrich, HPA021241), PEPCK2 (Cell Signalling Technology, 6924S) and MTHFD1L (Proteintech, 16113-1-AP). All antibodies were used at 1:1000 dilution unless stated otherwise. Secondary antibodies: IRDye 680RD Goat Anti-Mouse IgG (H + L) (926-68070) and IRDye 800CW Donkey Anti-Rabbit IgG (H + L) (926-32213) from LI-COR (used in a 1:10,000 dilution)..

Flow cytometry analysis of Apoptosis

250,000 cells (MDA-MB-468, B16-F10 and A375) or 200,000 cells (4T1) were seeded in 6-well plate, allowed to attach overnight and treated as indicated for 48h. At endpoint, medium was collected, cells were washed with PBS and PBS was collected followed by cell trypsinisation. Cells were pelleted and washed with ice-cold

536 PBS. Each sample was stained for 15 min on ice and in the dark with 50 µL AnnexinV staining solution (5 %
537 AnnexinV-FITC antibody in AnnexinV binding buffer (10 mM HEPES pH 7.4, 140 mM NaCl, 2.5 mM $CaCl_2$, 0.1
538 % BSA in ^{MQ}water)). Directly prior to measurements, 450 µL of propidium iodide (PI) staining solution was
539 added (11.1 µg/ml in AnnexinV binding buffer). Measurements were done using NovoCyte Quanteon
540 (Agilent) and software NovoExpress (version 1.5.0). FlowJo version 10.6.2 was used for analysis.

541 **Proliferation assays**

542 Cells were seeded at a concentration of 25,000 cells/well in a 12-well plate or 12,500 cells/well in a 24-well
543 plate in triplicates. Separate triplicate wells were counted when treatment was added to set 0h count for
544 fold change calculations. Medium and treatment were replaced at 48h and 72h. At endpoint, cells were
545 trypsinised and viable cell count was obtained using Countess™ automated counter (Thermo Fisher).

546 **Anchorage Independent 3D growth assays**

547 Cells were cultured in ultra-low attachment flask (Greiner) for a minimum of five days. Cells were collected
548 and spun at 100 RCF for 5 min and afterwards resuspended in Ca^{+2} and Mg^{+2} free PBS. 5,000 cells were seeded
549 in 96-well ultra-low attachment plates (S-Bio or facellitate) already in the experimental medium and the
550 plates were spun at 100 RCF for 10 minutes. 3D growth was determined using IncuCyte® S3 Live-Cell Analysis
551 system (Sartorius) over the indicated time periods.

552 **RNA extraction, cDNA synthesis and RT-qPCR**

553 300,000 cells were seeded in 6-well plate and treated for 24h as indictaed in the figures. RNA was extracted
554 directly from the plates using RNeasy Mini Kit (Qiagen, 74104). 2µg of RNA were used for cDNA synthesis
555 using High Capacity cDNA Reverse Transcription Kit (Thermo Fischer Scientific, 4368814). For qPCR, we used
556 Fast SYBR™ Green Master Mix (Thermo Fischer Scientific, 4368814) with 20 ng cDNA/sample in duplicates
557 and the reaction was conducted at 95°C for 20 s followed with 40 cycles of 95°C for 1 s and 60°C for 20 s. The
558 QuantStudio 5 Real-Time PCR System was used (Applied Biosciences, ThermoFisher Scientific). CT values
559 were determined by QuantStudio Design and Analysis v1.5.1 software (Applied Biosciences, ThermoFisher
560 Scientific). Primers used in this study are listed in Table S1.

Targeted gene	Species	Forward primer sequence	Reverse primer sequence
Psph	Mouse	AGATTTCCCAGGGATCCGGC	CAGTCCTCACTCAAGGCTCG
Psat1	Mouse	CCCAGCTGTGCGGAATGAGA	GAGCACACTGATGCCGAGTC
Phgdh	Mouse	CAGTGCAAGAAAGGTGTGCG	TTCTCGTGGTCCACTAAGGC
Shmt1	Mouse	TGCCCTCCCCATTTGAACAC	ATCTCTTTGCCAGTCTTGGGAT
Shmt2	Mouse	CTGCACAGTGGGGAGTCAAT	GTCAGTGCCAGGTTGAGCTT
Mthfd2	Mouse	CTGCGTTGGCTGTGCGGTT	CTGAGGTGTGGCCGCTTGT
Mthfd1	Mouse	CGTGGGTGGCAGACTAGCAA	TACCTGCTCCTGCATCCGAG
Aldh1l1	Mouse	TAGCAGGTGCCTTCCAACCT	CTTAAACACGGGCACGCCAT

Aldh1l2	Mouse	TTGACAGCCCAAAGCATGGC	CTGCCCAGAAAACAGAAAACCCA
Gapdh	Mouse	CATCACTGCCACCCAGAAGACTG	ATGCCAGTGAGCTTCCCGTTCAG

Supplementary Table 1. List of primers used in this study and their sequences.

Metabolomics

Stable Isotope Tracing and Metabolite Extraction

- ***In vitro* tracing and metabolite extraction:**

Stable isotope tracing experiments with [U-^{13}C] glucose, [U-^{13}C] galactose, [U-^{13}C] glutamine, [U-^{13}C] serine (Cambridge Isotope Laboratories, CLM-1396, CLM-1570, CLM-1822 and CLM-1574 respectively) and [U-^{13}C] lactate (Sigma Aldrich, 485926) were performed in DMEM (Thermo Fisher Scientific, 1443001), RPMI 1640 for SILAC (Thermo Fisher Scientific, 88365), Advanced DMEM/F12 for SILAC (Thermo Fisher Scientific, A2494301) or customised DMEM (Thermo Fisher Scientific) depending on the cell lines used. These tracer mediums were supplemented with the missing metabolites according to the experimental setup to mimic the original formula of DMEM, RPMI 1640 or advanced DMEM/F12. For sodium [U-^{13}C] lactate 5 mM final concentration was used. For glucose and galactose tracing 10% normal FBS was used while for the rest we used 10% dialysed FBS. Experimental set-up and extraction of metabolites for GC-MS analyses was done as described in [52]. Metabolite extraction for LC-MS was done as described in [24]. Metabolite extraction for IC-MS was identical to LC-MS.

- ***In vivo* metabolite extraction**

Metabolite extraction from tumours, spleen and plasma was performed as detailed in [24]. For B cells separated from the spleen, cells were washed with ice-cold PBS and subsequently 40 µL/1 million cells extraction fluid [acetonitrile/$^{MQ}H_2O$/methanol (ratio, 3:2:5); liquid chromatography–MS (LC-MS) grade solvents)] was added to each cell pellet. Cells were mixed for 10 min on a thermomixer at 4°C at maximum speed, then the tubes were centrifuged for 10 min at 16,100 RCF at 4°C. 50 µL of the supernatant was collected and transferred to an already-cooled LC-MS glass vial with inserts and stored at -80°C until measurement.

YSI measurements and medium exchange rates:

Medium samples were filtered (PVDF, 0.22 µm) prior measurement to remove particulates.

Absolute quantitative values for lactic acid and glutamine were acquired using a YSI 2950D Biochemistry Analyzer (Kreienbaum KWM). The instrument was calibrated and prepared according to the manufacturers' instruction. For a precise and reliable quantification, external concentration curves of each target compound were prepared and measured in triplicates. Absolute uptake and release rates were calculated as described in [24].

GC-MS measurements

- Formate measurements

Formate was derivatized to benzyl formate from the collected medium samples using the MCF protocol described in [24]. GC-MS analysis was performed using an Agilent 7890 A GC coupled to an Agilent 5975 C inert XL Mass Selective Detector (Agilent Technologies). A sample volume of 1 µL was injected into a Split/Splitless inlet, operating in split mode (20:1) at 280 °C. The gas chromatograph was equipped with a 30 m (I.D. 250 µm, film 0.25 µm) ZB-5MSplus capillary column (Phenomenex, 7HG-G030-11-GGA) plus 5 m GUARDIAN in front of the analytical column. Helium was used as carrier gas with a constant flow rate of 1.4 ml/min. GC oven temperature was held at 90 °C for 1 min and increased to 115 °C at 10 °C/min followed by 20 °C/min to 160 °C and a post run time of 4.25 min at 325 °C. Total run time was 10 min. Transfer line temperature was set to 280 °C. Mass selective detector (MSD) was operating under electron ionization at 70 eV. MS source was held at 230 °C and the quadrupole at 150 °C. For precise quantification, measurements were performed in selected ion monitoring mode. Target ions (m/z) and dwell times are listed below in Table S2. GC-MS chromatograms were processed using Agilent MassHunter Quantitative Analysis for GC-MS, Version B.08.00. Natural isotope correction and analysis of formate release rates was done as previously described in [24].

Derivative (Metabolite)	Quant-Ion (m/z)	Dwell Time (ms)
Benzyl Formate M_0	136.1	40
Benzyl Formate M_1	137.1	40
IS-Benzyl Formate (^{13}C,D) M_0	138.1	40
IS-Benzyl Formate (^{13}C,D) M_1	139.1	40
IS-Benzyl Formate(^{13}C,D) M_2	140.1	40

Supplementary Table 2. Dwell times and quantification ions for the derivatized formate.

- Intracellular metabolites measurements (Fig. S3A-B)

First, dried polar extracts were derivatized for 90 min at 55 °C with 20 µl of methoxyamine (c = 20 mg/ml) in pyridine under continuous shaking and subsequently for 60 min at 55 °C with additional 20 µl of MTBSTFA w/ 1% TBDMCS. GC-MS analysis was performed using an Agilent 7890B GC coupled to an Agilent 5977 A Mass Selective Detector (Agilent Technologies). A sample volume of 1 µl was injected into a Split/Splitless inlet, operating in splitless mode at 270 °C. Gas chromatograph was equipped with a 30 m (I.D. 250 µm, film 0.25 µm) ZB-35MS capillary column with 5 m guard column (Phenomenex). Helium was used as carrier gas with a constant flow rate of 1.2 ml/min. GC oven temperature was held at 100°C for 2 min and increased to 300°C at 10°C/min and held for 4 min. Total run time was 26 min. Transfer line temperature was set to 280°C. Mass selective detector (MSD) was operating under electron ionization at 70 eV. MS source was held at 230°C and the quadrupole at 150 °C. For precise quantification of the MID, measurements were performed in selected ion monitoring mode. The derivative measured here was pyruvic acid 1MeOX 1TBDMS with target

ions 174.0 – 180.1 [M-57 fragment] and dwell times of 15 ms. The MetaboliteDetector software package (Version 3.220180913) was used for mass spectrometric data post processing, quantification, MID calculations, correction of natural isotope abundance, and determinations of fractional carbon contributions [53].

IC-MS measurements (Fig. 1C-I, S6F-H)

For the IC-MS measurements, polar extracts were analyzed as previously described [54] with the following adjustments. 50-75% of the total polar extract was dried overnight under vacuum. Dried polar metabolite pellets were reconstituted in 25 µl of nanopure water (Milli-Q Advantage A10) of which 20 µl was injected. For the ICMS system, we interfaced a Dionex ICS-6000+ ion chromatograph with a QExactive high resolution mass spectrometer (both Thermo Fisher Scientific). The guard, column, gradient settings, and suppressor type remained unchanged [54]. The heated electrospray ionization (HESI) settings were as follows: spray voltage of 2.500 kV, auxiliary gas temperature of 420 °C, seep gas flow rate of 0, auxiliary gas flow rate of 15 units, and sheath gas flow rate of 50 units. The settings for acquisition of MS1 data were: m/z scan range of 80-750, resolution of 17.5 K, automatic gain control (AGC) target of 1e6, and maximum injection time of 100 milliseconds. Data were acquired using two micro-scans.

LC-MS Measurements

Metabolite analyses were performed using a Vanquish Flex LC coupled to a Q Exactive HF mass spectrometer (Thermo Scientific). Chromatography was carried out with a SeQuant ZIC-pHILIC 5 µm polymer (150 x 2.1 mm) column with corresponding SeQuant ZIC-pHILIC Guard (20 x 2.1 mm) pre-column. Column temperature was maintained at 45°C. The flow rate was set to 0.2 ml/min and the mobile phases consisted of 20 mmol/L ammonium carbonate in water, pH 9.2 (Eluent A) and Acetonitrile (Eluent B). The gradient was: 0 min, 80% B; 2 min, 80% B; 17 min, 20% B; 18 min 20% B; 19 min 80 % B; 20 min 80% B (0.4ml/min); 24 min 80% B (0.4ml/min); 24.5 min 80% B. The injection volume was 5 µL. All MS experiments were performed using electrospray ionization with polarity switching enabled (+ESI/-ESI). The source parameters were applied as follows: sheath gas flow rate, 25; aux gas flow rate, 15; sweep gas flow rate, 0; spray voltage, 4.5 kV (+) / 3.5 kV (–); capillary temperature, 325°C; S-lense RF level, 50; aux gas heater temperature, 50°C. The Orbitrap mass analyzer was operated at a resolving power of 30,000 in full-scan mode (scan range: *m/z* 75…1000; automatic gain control target: 1e6; maximum injection time: 250 ms).

Data from IC-MS and LC-MS measurements were acquired with Thermo Xcalibur software (Version 4.3.73.11) and analyzed with TraceFinder (Version 4.1). Natural isotope subtraction and subsequent analysis were performed as previously described using in house scripts [24].

<u>Oxygen consumption rate measurements</u>

10,000 cells (MDA-MB-468, 4T1 and MDA-MB-231) or 20,000 cells (HCT116) were seeded into 96-seahorse microplate (Agilent) on D-1. After attachment, glucose and galactose medium were added and cells were

incubated for 24h. Basal OCR was measured using XF96 Extracellular Flux Analyzer (Seahorse bioscience, Agilent) following the manufacturer's protocol, Wave 2.6.0 software was used for analyses. OCR was normalised by the protein concentration of the corresponding wells following the protocol described in[55] and using a Bradford assay.

660 **Figure 1**

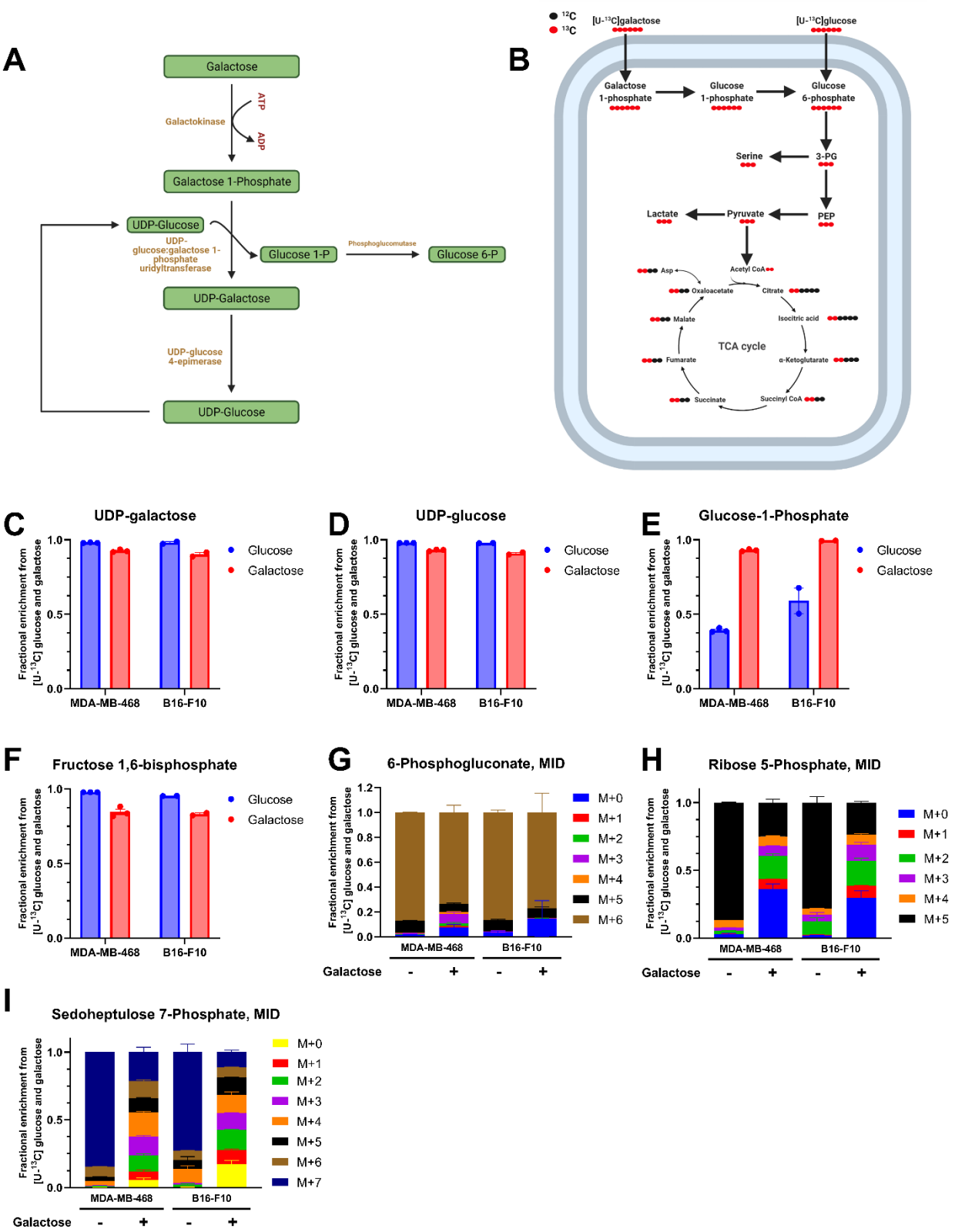

661

Figure 1. Cancer cells metabolize galactose and utilize it to support early glycolysis. A Schematic representation of Leloir pathway for galactose metabolism. **B** Schematic representation of the expected labelling pattern of simplified central carbon metabolism when using [U-^{13}C] glucose and [U-^{13}C] galactose tracer. **C-F** ^{13}C fraction from [U-^{13}C] glucose and [U-^{13}C] galactose into UDP-galactose **(C)**, UDP-glucose **(D)**, glucose 1-phosphate **(E)** and fructose 1,6-bisphosphate **(F)** after 24h incubation. **G-I** Fractional enrichment in 6-phosphogluconate **(G)**, ribose 5-phosphate **(H)** and sedoheptulose 7-phosphate **(I)** from [U-^{13}C] glucose and [U-^{13}C] galactose after 24h incubation. Data shown is mean±SEM of 3 (MDA-MB-468) or 2 (B16-F10) independent experiments each being the average of 3 different replicate wells. (**C-F**) Each dot represents an independent experiment averaged from 3 different replicate wells unless stated otherwise. (**C-F**) Mean±SEM, * $p<0.05$, ** $p<0.01$, *** $p<0.001$, **** $p<0.0001$, n.s. $p>0.1$. *P* value is calculated by Student's t-test, two-tailed, unpaired with Welch's correction unless stated otherwise.

673 **Figure 2**

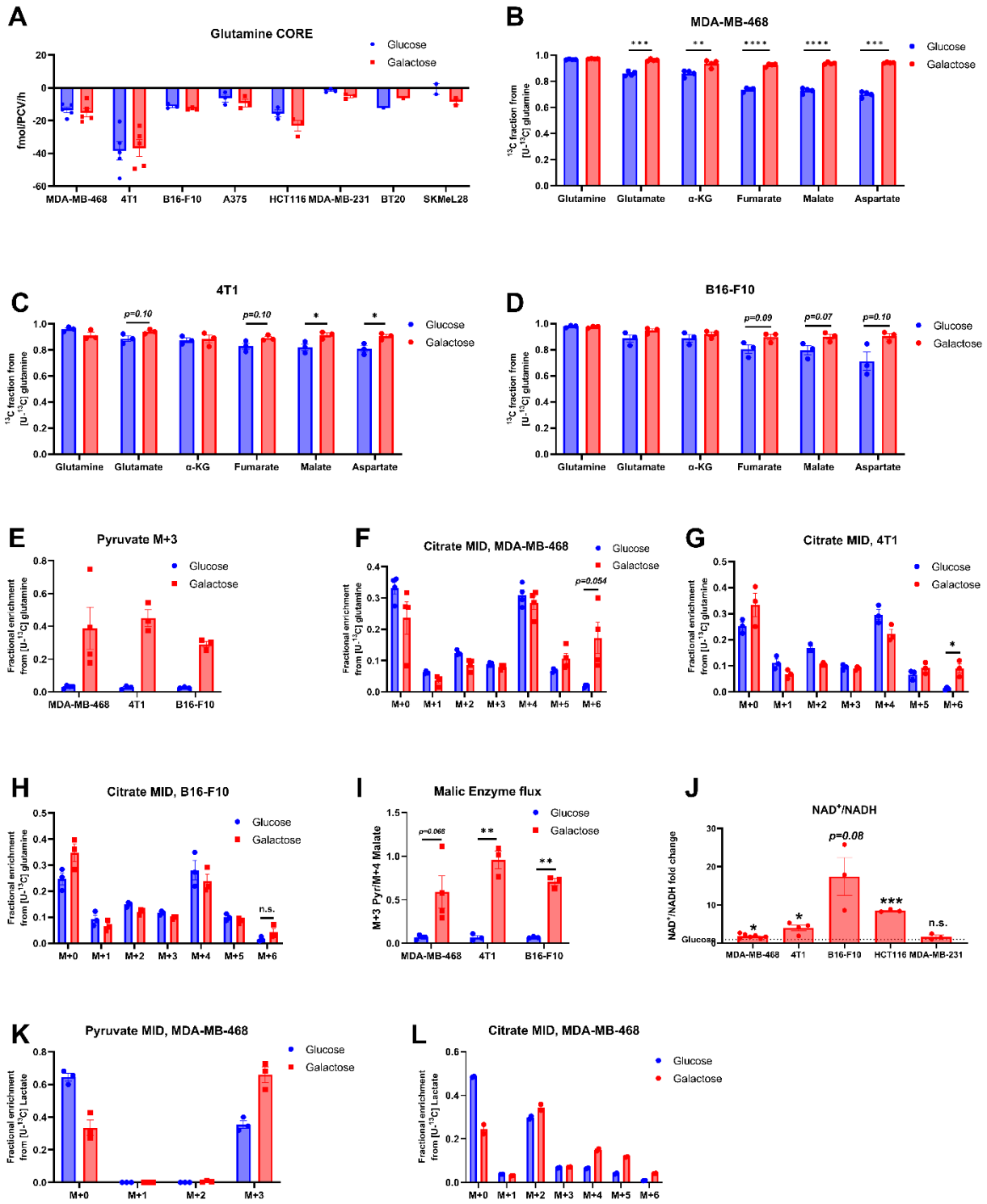

674

675 **Figure 2. Glutamine and lactate maintain upregulated oxidative TCA cycle function in reliance on malic enzyme (ME).**

676 **A** Absolute quantification of glutamine release from multiple cancer cell lines after 24h incubation with either glucose

677 or galactose. **B-D** ^{13}C fraction in TCA cycle metabolites from [U-^{13}C] glutamine after 24h incubation with either glucose

or galactose medium in MDA-MB-468 **(B)**, 4T1 **(C)** and B16-F10 **(D)**. **E** Fractional enrichment in M+3 pyruvate from [U-^{13}C] glutamine after 24h incubation with either glucose or galactose medium in MDA-MB-468, 4T1 and B16-F10. **F-H** Fractional enrichment in citrate from [U-^{13}C] glutamine after 24h incubation with either glucose or galactose medium in MDA-MB-468 **(F)**, 4T1 **(G)** and B16-F10 **(H)**. **I** Malic enzyme flux ratio calculated as M+3 pyruvate/M+4 malate isotopologues from [U-^{13}C] glutamine after 24h incubation with either glucose or galactose medium in MDA-MB-468, 4T1 and B16-F10. **J** NAD^+/NADH ratio measured with LC-MS in the indicated cancer cell lines after 24h incubation with galactose and normalised to the same ratio with 24h incubation with glucose. **K-L** Fractional enrichment in pyruvate **(K)** and citrate **(L)** from 5mM [U-^{13}C] sodium lactate after 24h incubation with either glucose or galactose medium in MDA-MB-468. (**A-L**) Each dot represents an independent experiment averaged from 3 different replicate wells unless stated otherwise. (**A-L**) Mean±SEM, * $p<0.05$, ** $p<0.01$, *** $p<0.001$, **** $p<0.0001$, n.s. $p>0.1$. *P* value is calculated by Student's t-test, two-tailed, unpaired with Welch's correction unless stated otherwise.

690 **Figure 3**

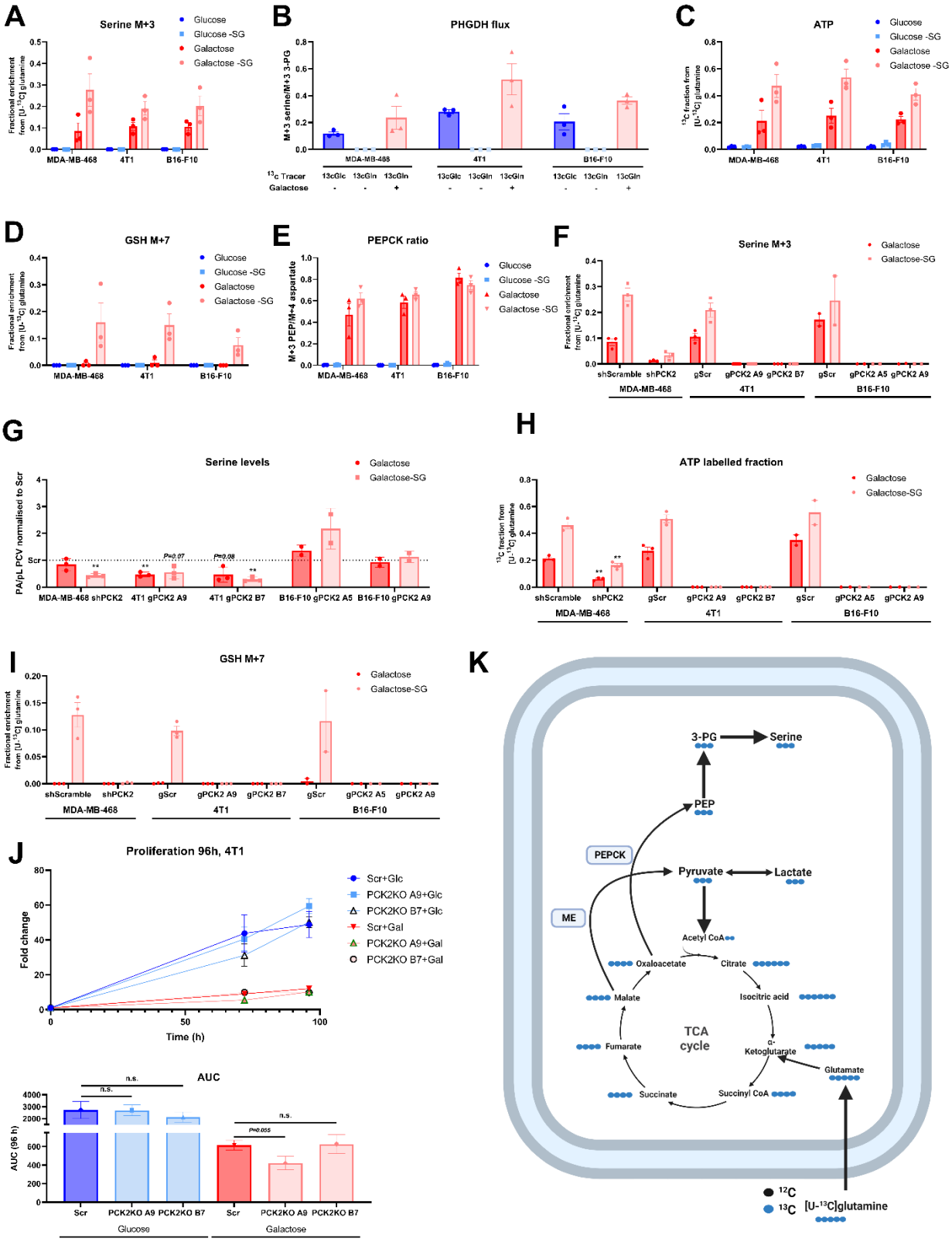

691

Figure 3. Glutamine metabolism is redirected towards SSP under glycolytic limitation via PEPCK. A Fractional enrichment in M+3 serine from [U-^{13}C] glutamine after 24h incubation with either glucose ± serine and glycine (SG) or galactose ± SG medium in MDA-MB-468, 4T1 and B16-F10. **B** Phosphoglycerate dehydrogenase (PHGDH) enzyme flux ratio calculated as M+3 serine/M+3 3-PG isotopologues from [U-^{13}C] glucose or glutamine (either with glucose or galactose) after 24h incubation in MDA-MB-468, 4T1 and B16-F10. **C** ^{13}C fraction in ATP from [U-^{13}C] glutamine after 24h incubation with either glucose ± SG or galactose ± SG medium in MDA-MB-468, 4T1 and B16-F10. **D** Fractional enrichment in M+7 glutathione (GSH) from [U-^{13}C] glutamine after 24h incubation with either glucose ± SG or galactose ± SG medium in MDA-MB-468, 4T1 and B16-F10. **E** Phosphoenolpyruvate carboxykinase (PEPCK) enzyme flux ratio calculated as M+3 PEP/M+4 aspartate isotopologues from [U-^{13}C] glutamine after 24h incubation with either glucose ± SG or galactose ± SG medium in MDA-MB-468, 4T1 and B16-F10. **F** Fractional enrichment in M+3 serine from [U-^{13}C] glutamine after 24h incubation with either glucose ± SG or galactose ± SG medium in MDA-MB-468 shScramble and shPCK2 cells, 4T1 and B16-F10 gScramble and gPCK2 cells. **G** Peak areas (PA) of intracellular serine in PCK2 KD/KOs normalised to packed cell volume (PCV) and presented as fold change to the levels in scramble cells. Data shown is for the levels measured in galactose ± SG medium. **H** ^{13}C fraction in ATP from [U-^{13}C] glutamine after 24h incubation with galactose ± SG medium and the comparison between scramble and PCK2 KD/KOs cells. **I** Fractional enrichment in M+7 glutathione (GSH) from [U-^{13}C] glutamine after 24h incubation with galactose ± SG medium and the comparison between scramble and PCK2 KD/KOs cells. **J** 2D proliferation curve of 4T1 gScramble and gPCK2 cells with either glucose or galactose, with the corresponding area under the curve (AUC). 72h timepoint includes 3 independent experiments while 96h includes 4 independent experiments (from at least 3 different replicate wells for each independent experiment). (**A-J**) Each dot represents an independent experiment averaged from 3 different replicate wells unless stated otherwise. (**A-J**) Mean±SEM, * $p<0.05$, ** $p<0.01$, *** $p<0.001$, **** $p<0.0001$, n.s. $p>0.1$. *P* value is calculated by Student's t-test, two-tailed, unpaired with Welch's correction unless stated otherwise. **K** Schematic representation of the rewiring of glutamine metabolism that take place under glycolytic limitation.

716 **Figure 4**

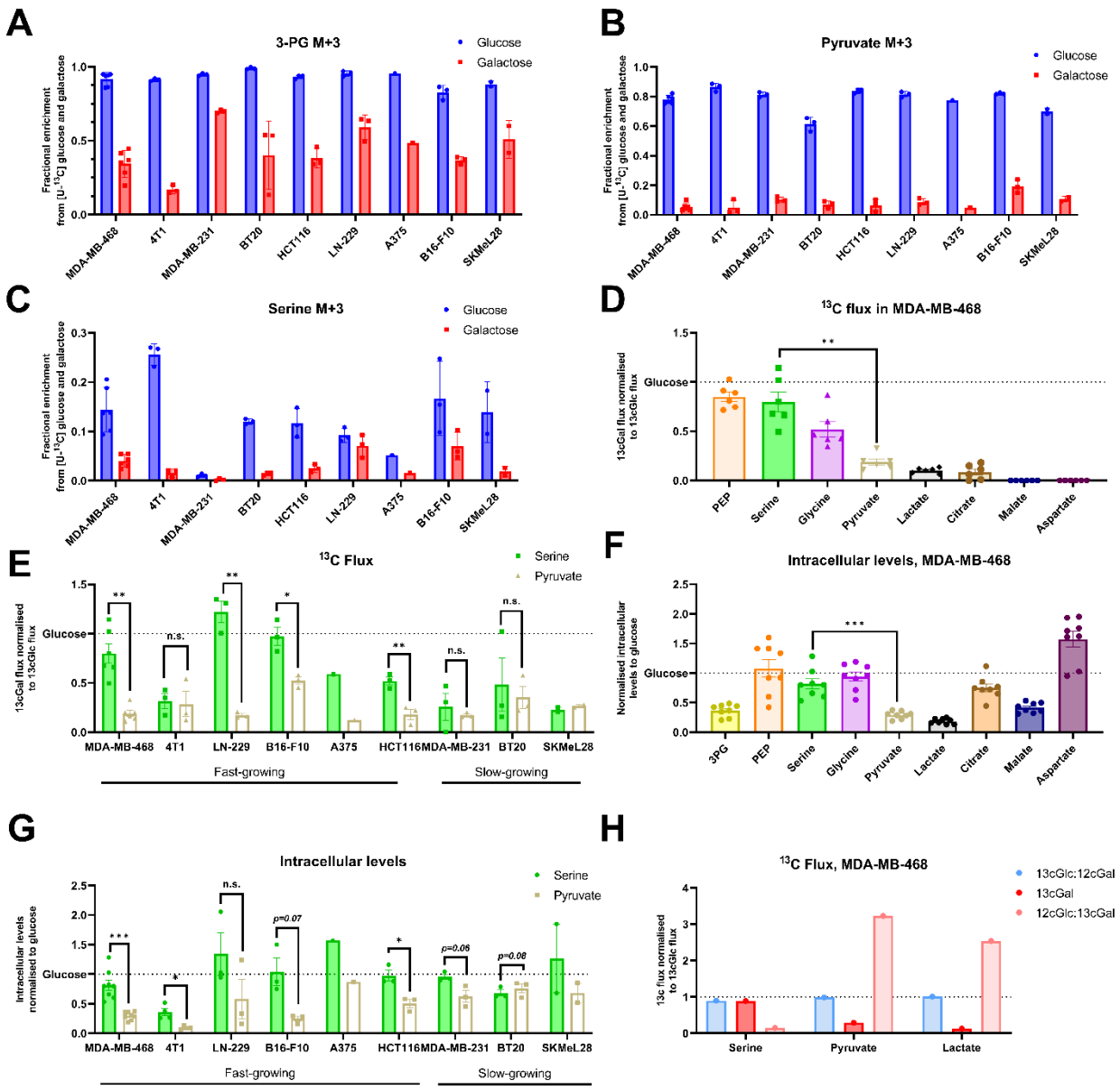

717

718 **Figure 4. Cancer cells sustain carbon flux towards serine synthesis pathway (SSP) under glycolytic limitation. A-C**
719 Fractional enrichment from 17.5 mM [U-^{13}C] glucose and galactose into M+3 3PG (**A**), M+3 pyruvate (**B**) and M+3 serine
720 (**C**) after 24h incubation measured with LC-MS. **D-E** The normalised relative ^{13}C flux under galactose towards multiple
721 metabolites represented as a fold change of the same ratio under glucose in MDA-MB-468 (**D**) and a panel of 9 cancer
722 cell lines (**E**). Fast-growing cells are those with doubling time <24h. **F-G** Intracellular levels of multiple metabolites under
723 galactose represented as a fold change of the levels under glucose in MDA-MB-468 (**F**) and a panel of 9 cancer cell lines
724 (**G**). **H** The normalised relative ^{13}C flux under galactose and glucose:galactose mixes towards multiple metabolites
725 represented as a fold change of the same ratio under glucose in MDA-MB-468. (**A-H**) Each dot represent an independent

experiment (from 3 different replicate wells). (**A-H**) Mean±SEM, * $p<0.05$, ** $p<0.01$, *** $p<0.001$, **** $p<0.0001$, n.s. $p>0.1$. *P* value is calculated by Student's t-test, two-tailed, unpaired with Welch's correction.

729 **Figure 5**

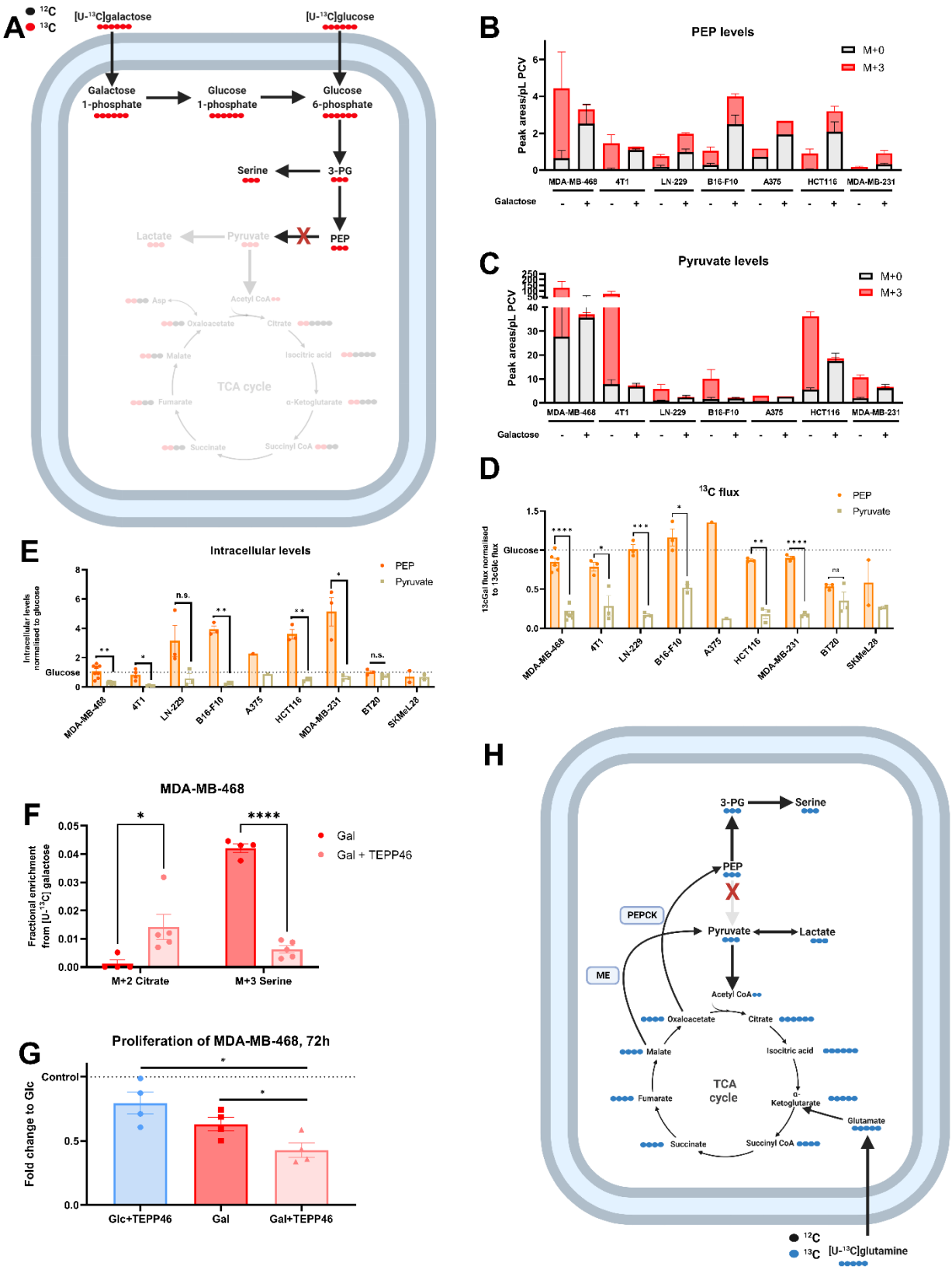

730

Figure 5. Glycolytic limitation inhibits glycolytic flux at pyruvate kinase isozyme M2 (PKM2). A Schematic representation of glycolysis and TCA cycle upon isotopologue labelling with [U-^{13}C] glucose and galactose with the proposed block at PKM2. **B-C** Peak areas of M+0 and M+3 isotopologues of PEP (**B**) and pyruvate (**C**) after 24h incubation with [U-^{13}C] glucose and galactose and normalisation to packed cell volume (PCV). **D** The normalised relative ^{13}C flux under galactose towards PEP and pyruvate represented as a fold change of the same ratio under glucose in a panel of 9 cancer cell lines. **E** Intracellular levels of PEP and pyruvate under galactose represented as a fold change of the levels under glucose in a panel of 9 cancer cell lines. **F** Fractional enrichment from [U-^{13}C] galactose into M+2 citrate and M+3 serine after 24h incubation (Gal+TEPP-46) as measured with LC-MS. **G** 2D proliferation of MDA-MB-468 treated with 100 µM of TEPP-46 with either glucose or galactose and measured as cell counts at 72h relative to proliferation under glucose. (**B**-**G**) Each dot represents an independent experiment (from at least 3 different replicate wells). (**B**-**G**) Mean±SEM, * $p<0.05$, ** $p<0.01$, *** $p<0.001$, **** $p<0.0001$, n.s. $p>0.1$. *P* value is calculated by Student's t-test, two-tailed, unpaired with Welch's correction. **H** Schematic representation of the rewiring of glutamine metabolism that take place under glycolytic limitation and the differentiation between ME and PEPCK2 fluxes.

745 **Figure 6**

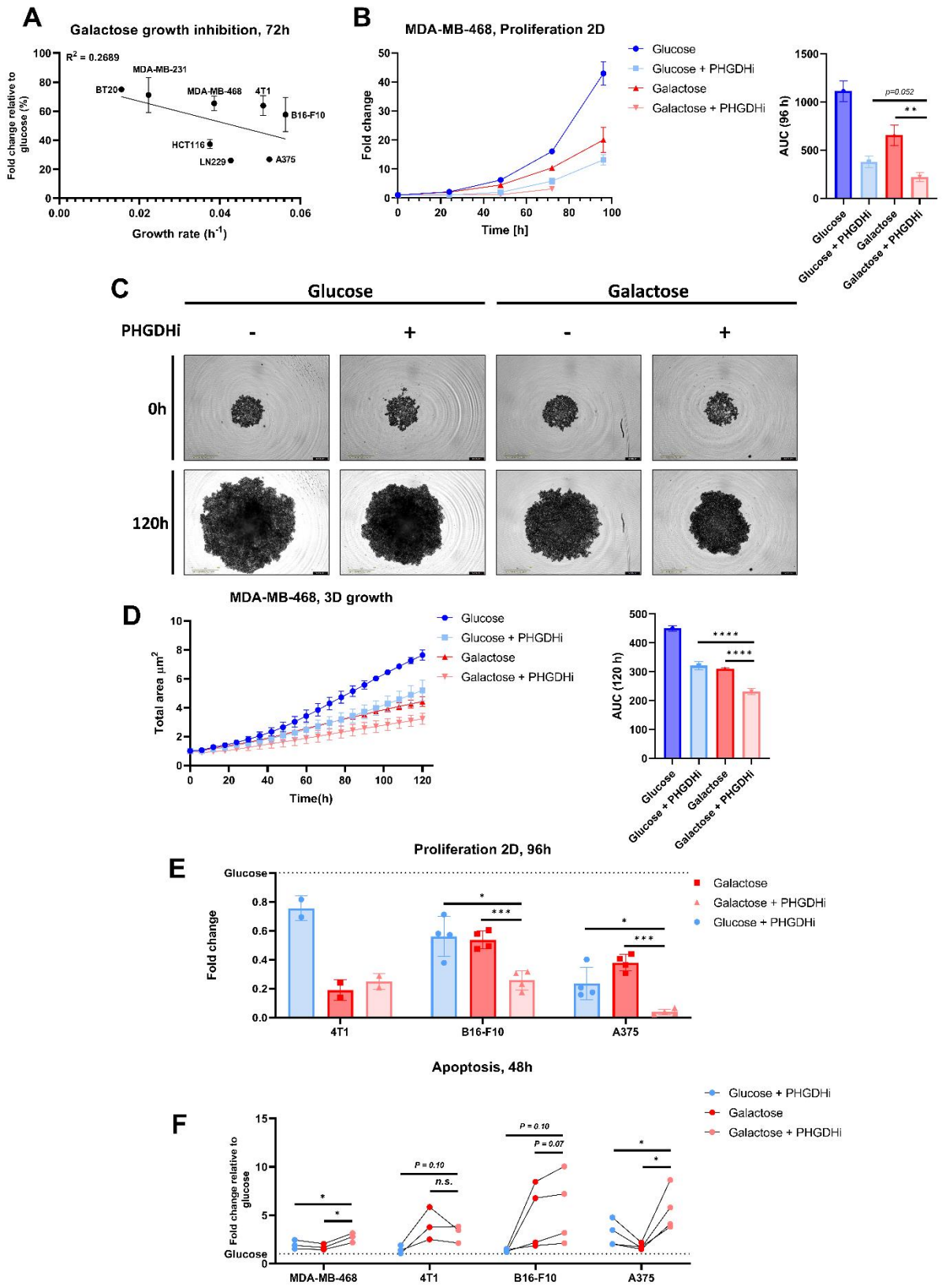

746

Figure 6. SSP is needed for proliferation and viability under glycolytic limitation. A The correlation between the growth rate of different cancer cell lines and the extent to which galactose inhibits their proliferation (represented as a percentage of growth under glucose). MDA-MB-468 n=5, 4T1 n=2, HCT116 n=2, MDA-MB-231 n=2, B16-F10 n=3, A375 n=3, BT20 n=1 and LN-229 n=1. R^2 measured for the line of best-fit using simple linear regression. **B** 2D proliferation of MDA-MB-468 when treated with 15 µM of the PHGDH inhibitor BI-4916 (PHGDHi) with either glucose or galactose, with the corresponding area under the curve (AUC). 24h and 96h timepoints include 4 independent replicates while 48h and 72h include 5 independent replicates (from at least 3 different replicate wells for each independent experiment). **C** Bright field images are representative of 3 independent experiments of MDA-MB-468 aggregates growing in anchorage-independent conditions. Scale bar represent 800 µM. **D** 3D growth of MDA-MB-468 aggregates using anchorage-independent conditions when treated with 15 µM of PHGDHi with either glucose or galactose, with the corresponding AUC. 3 independent experiments are represented each with at least 6 different replicate wells. **E** 2D proliferation of multiple cancer cell lines when treated with 15 µM of PHGDHi with either glucose or galactose as measured with cell counts at 96h relative to proliferation under glucose. Each dot represent an independent experiment from at least 3 different replicate wells. (**B**, **D, E**) Mean±SEM, * $p<0.05$, ** $p<0.01$, *** $p<0.001$, **** $p<0.0001$, n.s. $p>0.1$. *P* value is calculated by Student's t-test, two-tailed, unpaired with Welch's correction. **F** Viability of different cancer cell lines when treated with 15 µM of PHGDHi with either glucose or galactose for 48h as measured as annexin V^+ cells after excluding necrotic cells (PI). MDA-MB-468 and 4T1 n=3, B16-F10 and A375 n=4. Data shown is the mean, * $p<0.05$, ns $p>0.1$. *P* value is calculated by Student's t-test, two-tailed, paired.

766 **Figure 7**

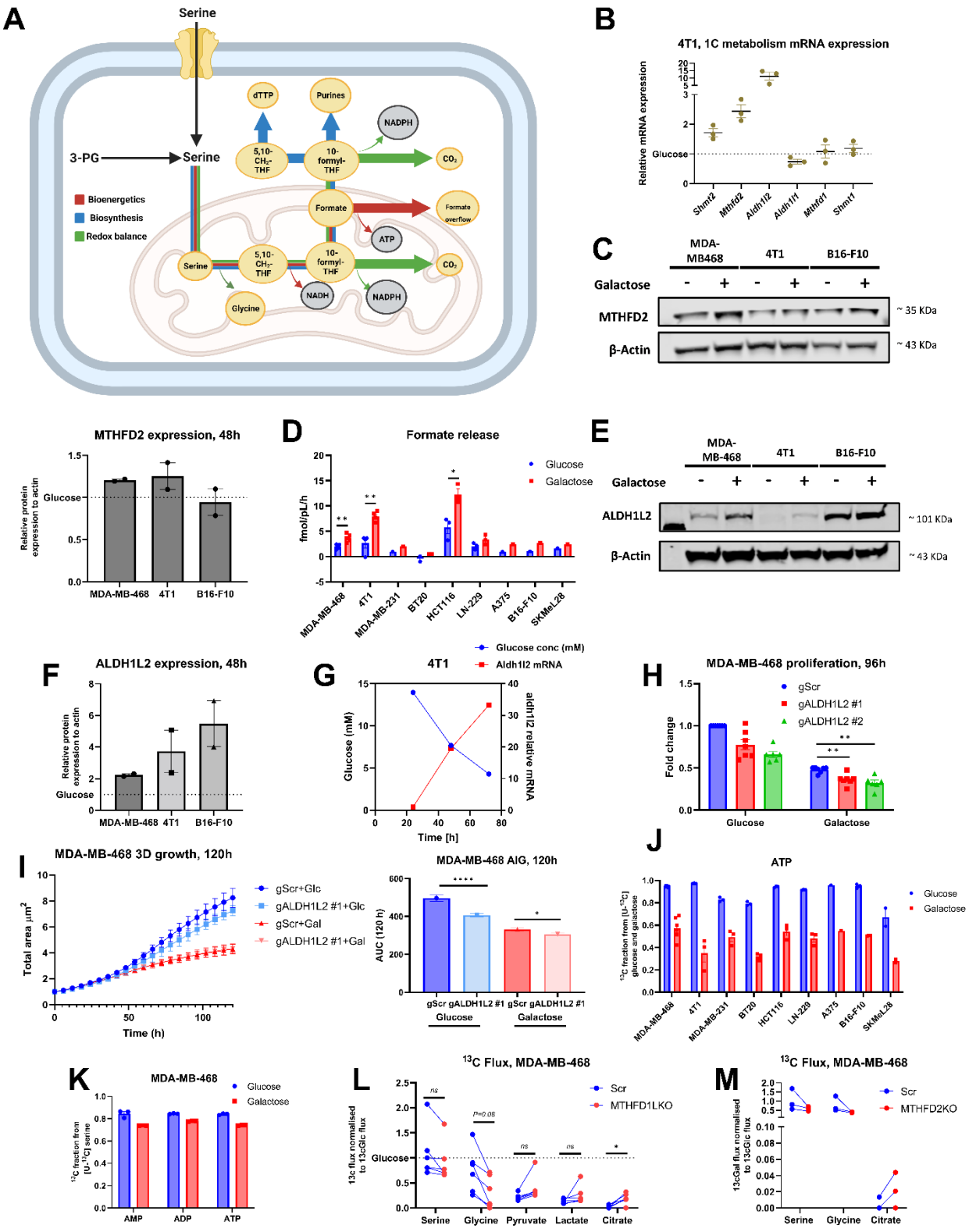

767

768 **Figure 7. SSP flux is crucial to sustain mitochondrial formate production to support all three metabolic pillars. A**
769 Schematic representation of the one-carbon cycle with the different pillars and how it can contribute to biosynthesis,
770 bioenergetic and redox balance. **B** mRNA expression of *Shmt2*, *Mthfd2*, *Aldh1l2*, *Aldh1l1, Mthfd1* and *Shmt1* genes
771 relative to *Gapdh* after 24h incubation with either glucose or galactose measured with RT-qPCR. Data presented as fold
772 change to the mRNA expression in cells cultured with glucose. **C** Protein expression of MTHFD2 after 48h incubation
773 with either glucose or galactose, with the quantification of these signals relative to β-actin as a loading control and
774 presented as a fold change of expression under galactose to that of glucose. **D** Absolute quantification of formate
775 release from the indicated cancer cell lines after 24h incubation with either glucose or galactose. **E** Protein expression
776 of ALDH1L2 after 48h incubation with either glucose or galactose, with the quantification of these signals relative to β-
777 actin as a loading control and presented as a fold change of expression under galactose to that of glucose. **G**
778 Concentration of glucose as measured in media in which 4T1 cells were cultured for 72h, compared to A*ldh1l2* mRNA
779 expression relative to *Gapdh* and presented as fold change for expression at 24h. mRNA was extracted from single wells
780 while medium measurement are mean±SEM of 3 different replicate wells. **H** 2D proliferation of MDA-MB-468 Scramble
781 and ALDH1L2 KOs cultured in either glucose or galactose as measured with cell counts at 96h relative to proliferation of
782 scramble cells under glucose. **I** 3D growth of MDA-MB-468 control and ALDH1L2KO aggregates using anchorage-
783 independent conditions in either glucose or galactose, with the corresponding AUC. 3 independent experiments are
784 represented each with at least 6 different replicate wells. **J** ^{13}C fraction in ATP from [U-^{13}C] glucose and galactose after
785 24h incubation in multiple cell lines. **K** ^{13}C fraction in AMP/ADP/ATP from [U-^{13}C] serine after 24h incubation in MDA-
786 MB-468. **L-M** The normalised relative ^{13}C flux under galactose towards multiple metabolites represented as a fold
787 change of the same ratio under glucose in MDA-MB-468 Scramble compared to MTHFD1LKO (**L**) and MTHFD2KO (**M**).
788 (**B-M**) Each dot represent an independent experiment averaged from 3 different replicate wells unless stated otherwise.
789 (**B-M**) Mean±SEM, * $p<0.05$, ** $p<0.01$, *** $p<0.001$, **** $p<0.0001$, n.s. $p>0.1$. *P* value is calculated by Student's t-test,
790 two-tailed, unpaired with Welch's correction unless stated otherwise.
791

792 **Figure 8**

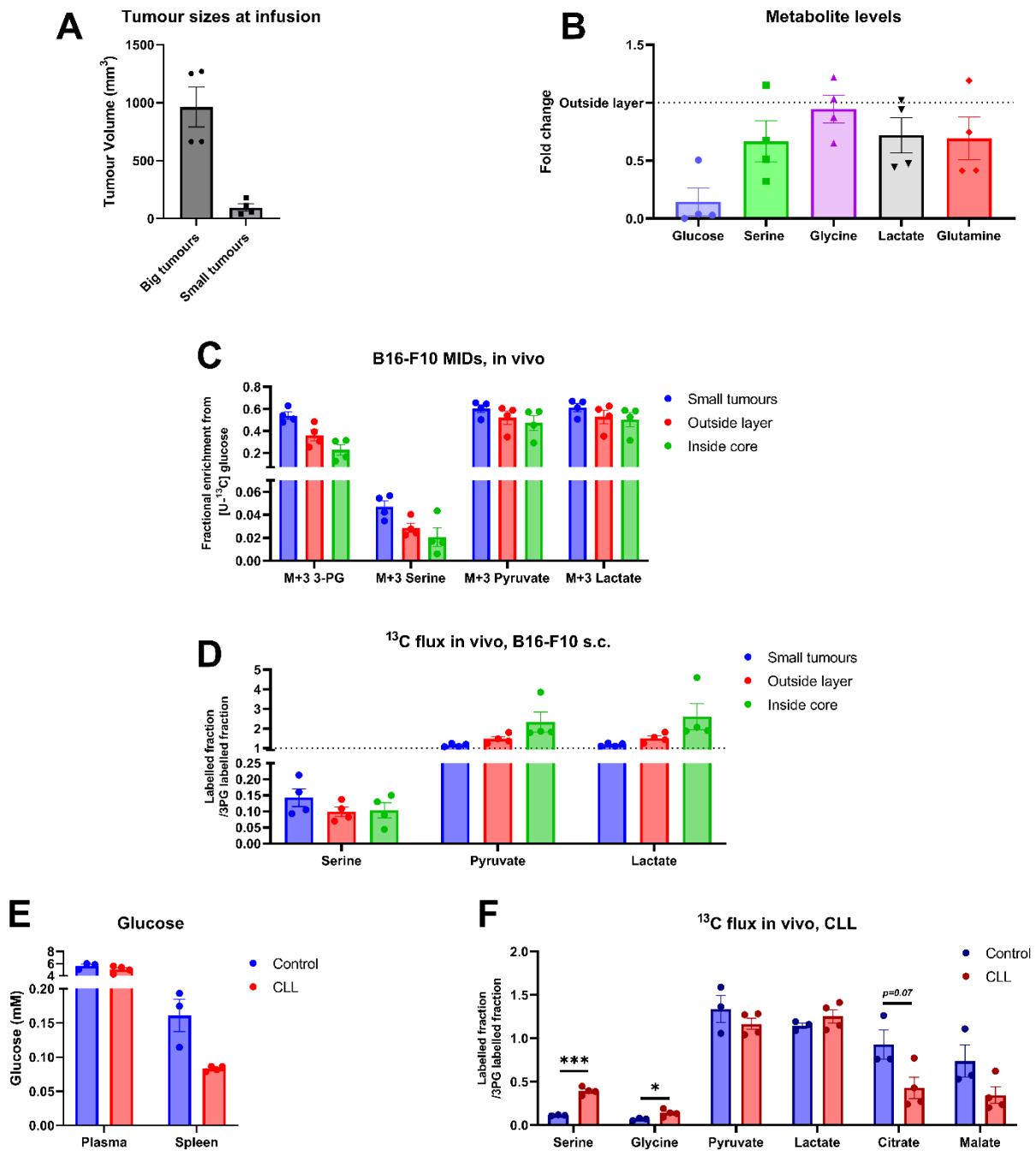

793

794 **Figure 8. *In vivo* relevance of using Gal to model glycolytic limitation**. **A** Tumour volume of B16-F10 tumours

795 grown subcutaneously on the flanks of C57BL/6 mice (n=4/group). **B** Metabolite levels measured from the inside core

796 of B16-F10 tumours and presented as fold change of the level of those metabolites in the outside layer of the same

797 tumours. **C** Fractional enrichment in tumour piece of the presented metabolites after 2h infusion with [U-^{13}C] glucose

798 via the tail vain. **D** The ^{13}C flux from 3PG towards multiple metabolites measured in B16-F10 tumours. **E** Glucose

concentration as measured in the plasma and in grinded spleen tissue from control and CLL mice after 2h continuous infusion with [U-^{13}C] glucose. The concentration was determined using standard addition method. **F** The ^{13}C flux from 3PG towards multiple metabolites measured in CLL cells collected from the spleen of CLL mice. (**A-F**) Each dot represent an biological replicate. (**A-F**) Mean±SEM, * $p<0.05$, ** $p<0.01$, *** $p<0.001$, **** $p<0.0001$, n.s. $p>0.1$. *P* value is calculated by Student's t-test, two-tailed, unpaired with Welch's correction unless stated otherwise.

805 **Figure S1**

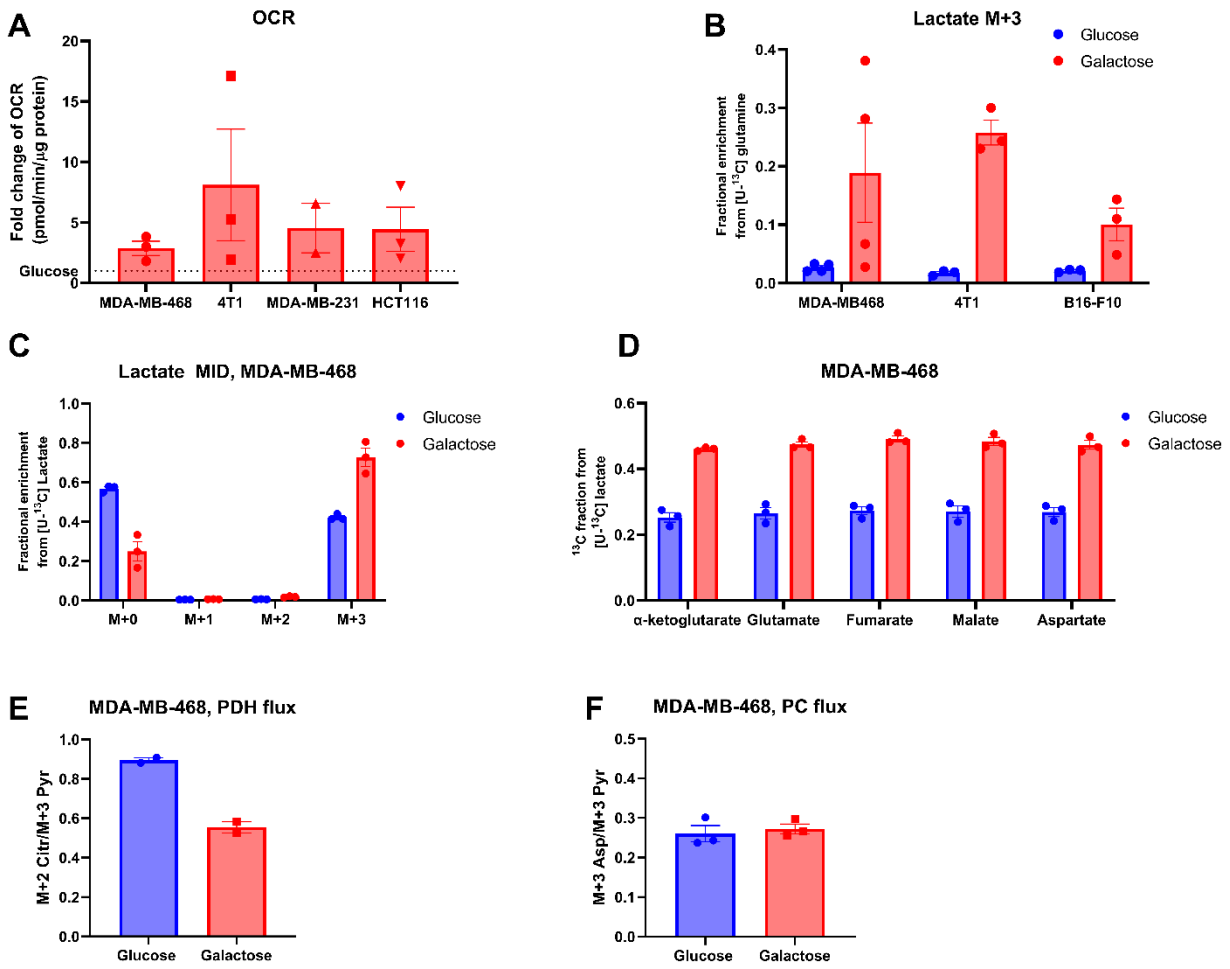

806

807 **Supplementary Figure 1. A** Basal oxygen consumption rate (OCR) measured by seahorse in 4 different cancer cell lines
808 after 24h incubation with galactose and presented as fold change to the same measurements with glucose. **B** Fractional
809 enrichment in M+3 lactate from [U-^{13}C] glutamine after 24h incubation with either glucose or galactose medium in
810 MDA-MB-468, 4T1 and B16-F10. **C** Fractional enrichment in lactate from [U-^{13}C] sodium lactate after 24h incubation
811 with either glucose or galactose medium in MDA-MB-468. **D** ^{13}C fraction in TCA cycle metabolites from [U-^{13}C] sodium
812 lactate after 24h incubation with either glucose or galactose medium in MDA-MB-468. **E** Pyruvate dehydrogenase (PDH)
813 enzyme flux ratio calculated as M+2 citrate/M+3 pyruvate isotopologues from [U-^{13}C] sodium lactate after 24h
814 incubation with either glucose or galactose medium in MDA-MB-468. **F** Pyruvate carboxylase (PC) enzyme flux ratio
815 calculated as M+3 aspartate/M+3 pyruvate isotopologues from [U-^{13}C] sodium lactate after 24h incubation with either
816 glucose or galactose medium in MDA-MB-468. (**A-F**) Each dot represents an independent experiment averaged from 3

817 different replicate wells. (**A-F**) Mean±SEM, * $p<0.05$, ** $p<0.01$, *** $p<0.001$, **** $p<0.0001$, n.s. $p>0.1$. *P* value is

818 calculated by Student's t-test, two-tailed, unpaired with Welch's correction.

819

820 **Figure S2**

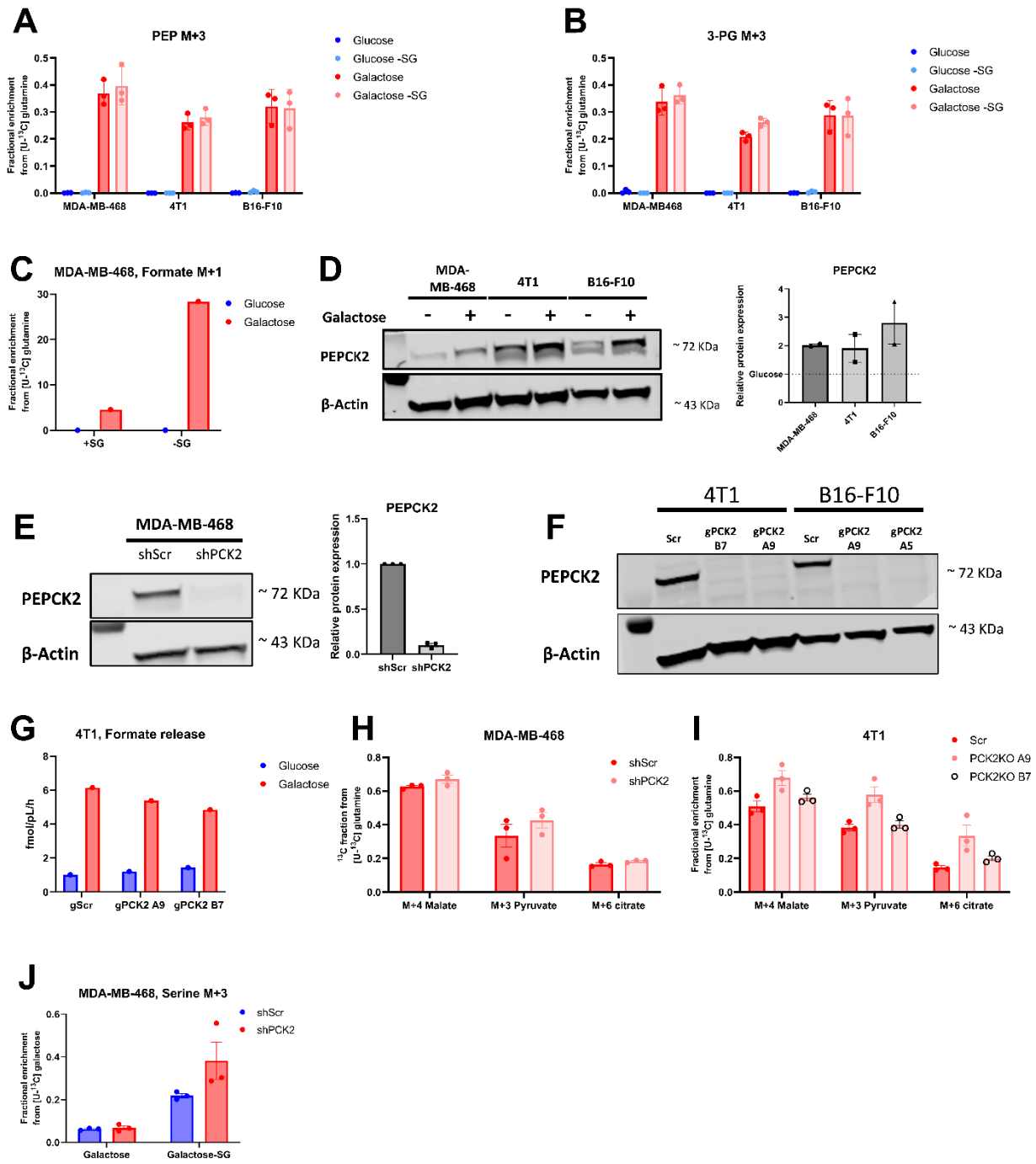

821

822 **Supplementary Figure 2. A-B** Fractional enrichment in M+3 PEP **(A)** and M+3 3-PG **(B)** from [U-^{13}C] glutamine after

823 24h incubation with either glucose ± serine and glycine (SG) or galactose ± SG medium in MDA-MB-468, 4T1 and B16-

824 F10. **C** Fractional enrichment in M+1 formate from [U-^{13}C] glutamine after 24h incubation with either glucose ±

825 serine and glycine (SG) or galactose ± SG medium in MDA-MB-468. **D** Protein expression of PEPCK2 after 48h incubation

with either glucose or galactose, with the corresponding quantification of signal intensities relative to β-actin as a loading control and presented as a fold change of expression under galactose to that of glucose. **E-F** Protein expression of PEPCK2 comparing scramble to PCK2 KD/KOs, with the corresponding quantification of these signals relative to β-actin as a loading control. **G** Absolute quantification of formate release from 4T1 after 24h incubation with either glucose or galactose. **H-I** Fractional enrichment in M+4 malate, M+3 pyruvate and M+6 citrate from [U-^{13}C] glutamine after 24h incubation with galactose + SG medium and comparison between control and MDA-MB-468 PCK2 KD **(H)** and 4T1 PCK2 KOs **(I)**. **J** Fractional enrichment in M+3 serine from [U-^{13}C] galactose after 24h incubation with galactose ± SG medium in MDA-MB-468 shScramble and shPCK2. (**A-J**) Each dot represents an independent experiment averaged from 3 different replicate wells replicate unless stated otherwise. (**A-J**) Mean±SEM, * $p<0.05$, ** $p<0.01$, *** $p<0.001$, **** $p<0.0001$, n.s. $p>0.1$. *P* value is calculated by Student's t-test, two-tailed, unpaired with Welch's correction unless stated otherwise.

838 **Figure S3**

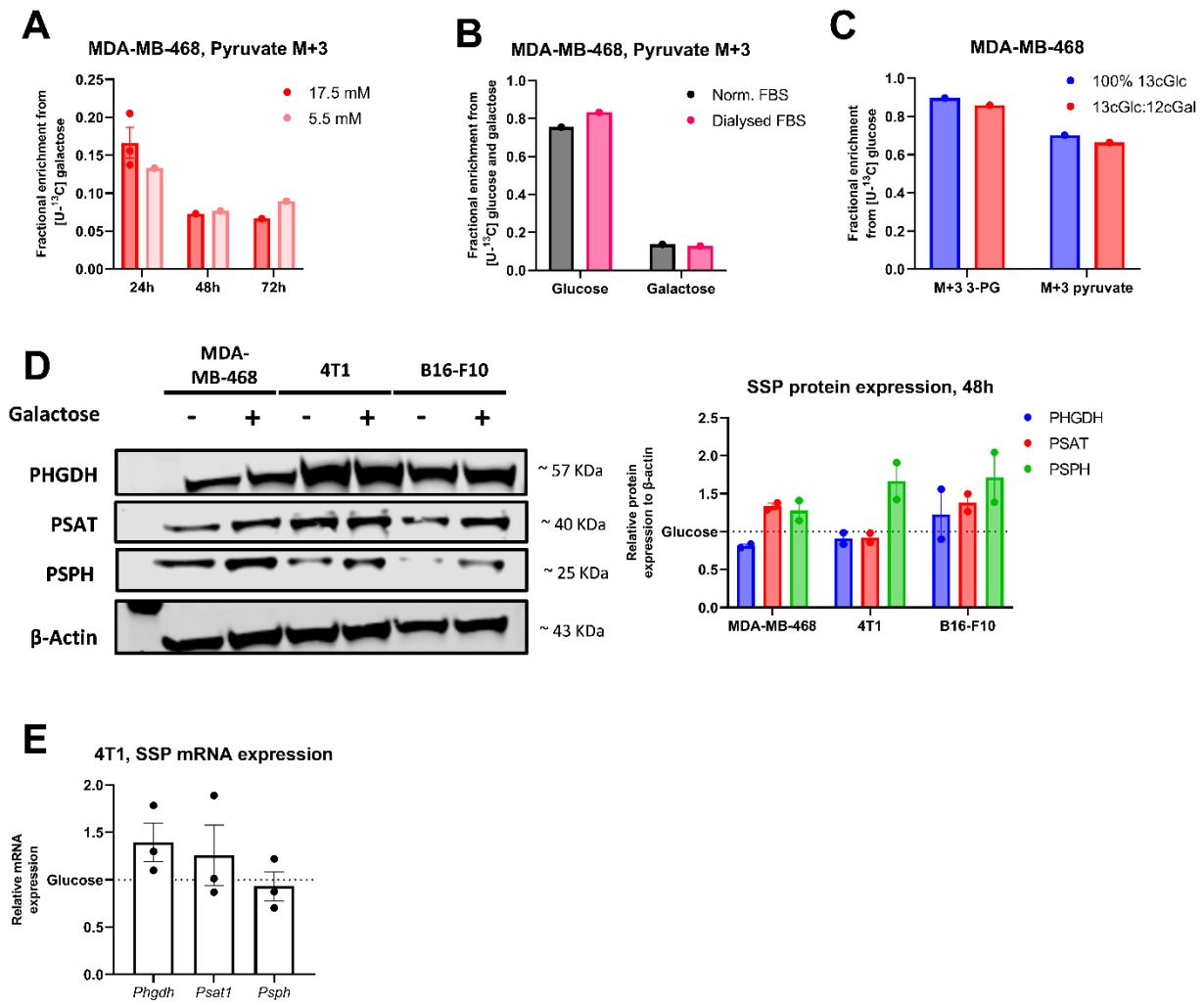

839

840 **Supplementary Figure 3. A** Fractional enrichment into M+3 pyruvate using [U-^{13}C] galactose after 24, 48, and 72 hour
841 incubation and using 17.5 or 5.5 mM of the tracer in MDA-MB-468. **B** Fractional enrichment into M+3 pyruvate using
842 [U-^{13}C] glucose and galactose after 24 hour incubation and using 17.5 mM of the tracer in MDA-MB-468 with 10% FBS
843 or 10% dialysed FBS. **C** Fractional enrichment from 17.5 mM [U-^{13}C] glucose into M+3 3PG and M+3 pyruvate after 24h
844 incubation measured with LC-MS. **D** Protein expression of PHGDH, PSAT and PSPH after 48h incubation with either
845 glucose or galactose, with the quantification of signal intensities relative to β-actin as a loading control and shown as a
846 fold change of expression under galactose to that of glucose. **E** mRNA expression of *Phgdh*, *Psat*, *Psph* relative to *Gapdh*
847 after 24h incubation with either glucose or galactose measured with RT-qPCR. Data presented as fold change to the
848 mRNA expression in cells cultured with glucose. (**A**-**E**) Each dot represent an independent experiment (**B**-**I** each

independent experiment is from at least 3 different replicate wells). (**A**-**E**) Mean±SEM, * $p<0.05$, ** $p<0.01$, *** $p<0.001$, **** $p<0.0001$, n.s. $p>0.1$. *P* value is calculated by Student's t-test, two-tailed, unpaired with Welch's correction.

852 **Figure S4**

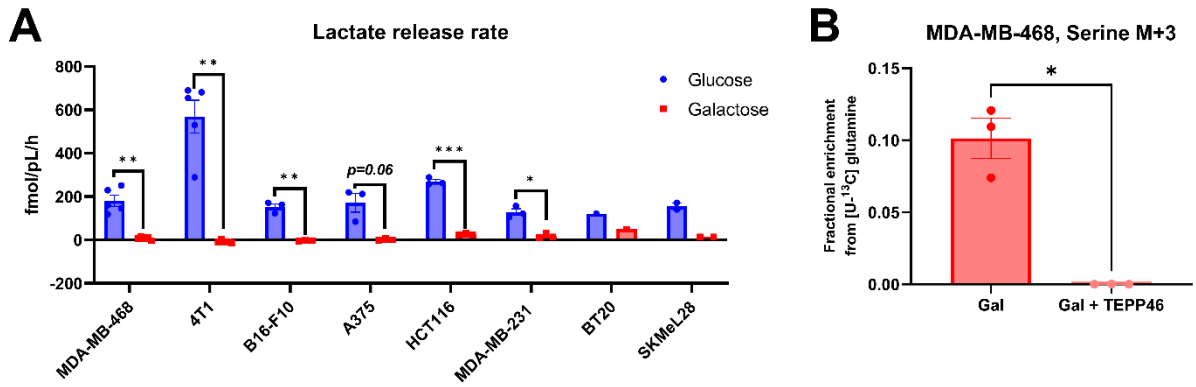

853

854 **Supplementary Figure 4. A** Absolute quantification of lactate released into the medium per hour of incubation with

855 normalisation to packed cell volume per condition in either glucose or galactose in multiple cancer cell lines. **B** Fractional

856 enrichment from [U-^{13}C] glutamine into M+3 serine after 24h incubation measured with LC-MS. (**A**-**B**) Each dot represent

857 an independent experiment (from 3 different replicate wells). (**A**-**B**) Mean±SEM, * p<0.05, ** p<0.01, *** p<0.001, ****

858 p<0.0001, n.s. p>0.1. P value is calculated by Student's t-test, two-tailed, unpaired with Welch's correction.

859

860 **Figure S5**

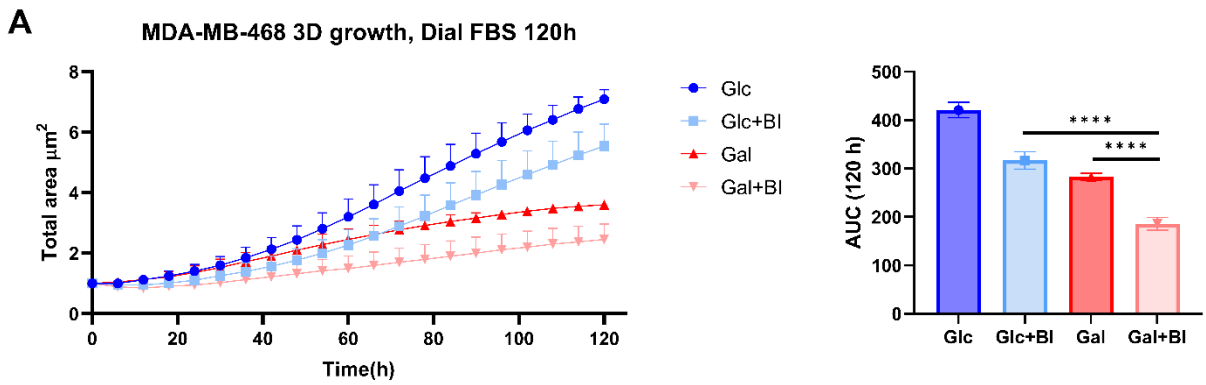

861

862 **Supplementary Figure 5. A** 3D growth of MDA-MB-468 aggregates using anchorage-independent conditions when

863 treated with 15 µM of PHGDHi with either glucose or galactose with 10% dialysed FBS, with the corresponding AUC. 3

864 independent experiments are represented each with at least 6 replicate wells. Mean±SEM, * $p<0.05$, ** $p<0.01$, ***

865 $p<0.001$, **** $p<0.0001$, n.s. $p>0.1$. *P* value is calculated by Student's t-test, two-tailed, unpaired with Welch's

866 correction.

867

868 **Figure S6**

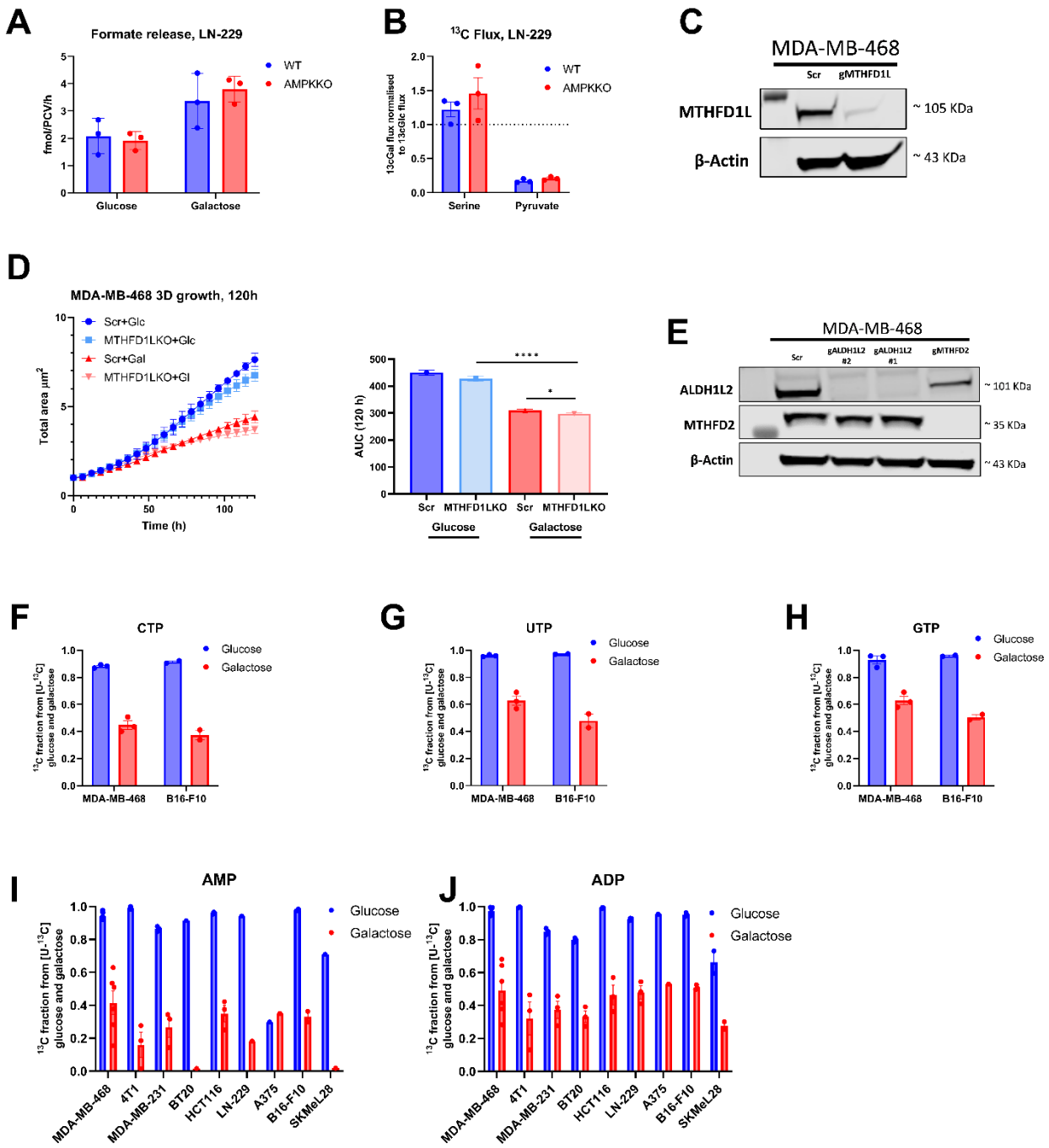

869

870 **Supplementary Figure 6. A** Absolute quantification of formate release from LN-229 control and AMPKKO after 24h
871 incubation with either glucose or galactose. **B** The normalised relative ^{13}C flux under galactose towards serine and
872 pyruvate is represented as a fold change of the same ratio under glucose in LN-229 control and AMPKKO. **C** Protein
873 expression of MTHFD1L comparing scramble to the corresponding KO with β-actin as a loading control. **D** 3D growth of
874 MDA-MB-468 control and MTHFD1LKO cell aggregates using anchorage-independent conditions in either glucose or

galactose, with the corresponding AUC. 3 independent experiments are represented each with at least 6 different replicate wells. **E** Protein expression of MTHFD2 and ALDH1L2 comparing scramble to the corresponding KOs with β-actin as a loading control. **F-H** Fractional enrichment in CTP **(F)**, UTP **(G)** and GTP **(H)** from [U-^{13}C] glucose and galactose after 24h incubation. Data shown is the mean±SEM of 3 (MDA-MB-468) or 2 (B16-F10) independent experiments each being the average of 3 different replicate wells. **I-J** ^{13}C fraction in AMP **(I)** and ADP **(J)** from [U-^{13}C] glucose and galactose after 24h incubation in multiple cell lines. (**A-B, F-J**) Each dot represent an independent experiment averaged from 3 different replicate wells unless stated otherwise. (**A-J**) Mean±SEM, * $p<0.05$, ** $p<0.01$, *** $p<0.001$, **** $p<0.0001$, n.s. $p>0.1$. *P* value is calculated by Student's t-test, two-tailed, unpaired with Welch's correction unless stated otherwise.

References:

1. Crabtree, H.G., *Observations on the carbohydrate metabolism of tumours.* Biochem J, 1929. **23**(3): p. 536-45.
2. Hanahan, D. and R.A. Weinberg, *Hallmarks of cancer: the next generation.* Cell, 2011. **144**(5): p. 646-74.
3. Warburg, O., *The Metabolism of Carcinoma Cells1.* The Journal of Cancer Research, 1925. **9**(1): p. 148-163.
4. Vander Heiden, M.G., L.C. Cantley, and C.B. Thompson, *Understanding the Warburg effect: the metabolic requirements of cell proliferation.* Science, 2009. **324**(5930): p. 1029-33.
5. Vazquez, A., et al., *Catabolic efficiency of aerobic glycolysis: The Warburg effect revisited.* BMC Systems Biology, 2010. **4**(1): p. 58.
6. Fernandez-de-Cossio-Diaz, J. and A. Vazquez, *Limits of aerobic metabolism in cancer cells.* Sci Rep, 2017. **7**(1): p. 13488.
7. Locasale, J.W., et al., *Phosphoglycerate dehydrogenase diverts glycolytic flux and contributes to oncogenesis.* Nat Genet, 2011. **43**(9): p. 869-74.
8. Osthus, R.C., et al., *Deregulation of glucose transporter 1 and glycolytic gene expression by c-Myc.* J Biol Chem, 2000. **275**(29): p. 21797-800.
9. Ying, H., et al., *Oncogenic Kras maintains pancreatic tumors through regulation of anabolic glucose metabolism.* Cell, 2012. **149**(3): p. 656-70.
10. Amendola, C.R., et al., *KRAS4A directly regulates hexokinase 1.* Nature, 2019. **576**(7787): p. 482-486.
11. de Alteriis, E., et al., *Revisiting the Crabtree/Warburg effect in a dynamic perspective: a fitness advantage against sugar-induced cell death.* Cell Cycle, 2018. **17**(6): p. 688-701.
12. Luengo, A., et al., *Increased demand for NAD(+) relative to ATP drives aerobic glycolysis.* Mol Cell, 2021. **81**(4): p. 691-707.e6.
13. Wang, Y., et al., *Saturation of the mitochondrial NADH shuttles drives aerobic glycolysis in proliferating cells.* Molecular Cell, 2022. **82**(17): p. 3270-3283.e9.
14. Bergers, G. and S.M. Fendt, *The metabolism of cancer cells during metastasis.* Nat Rev Cancer, 2021. **21**(3): p. 162-180.
15. Fendt, S.-M., C. Frezza, and A. Erez, *Targeting Metabolic Plasticity and Flexibility Dynamics for Cancer Therapy.* Cancer Discovery, 2020. **10**(12): p. 1797-1807.
16. Cantor, J.R., *The Rise of Physiologic Media.* Trends in Cell Biology, 2019. **29**(11): p. 854-861.
17. Díaz-Ruiz, R., et al., *Mitochondrial oxidative phosphorylation is regulated by fructose 1,6-bisphosphate. A possible role in Crabtree effect induction?* J Biol Chem, 2008. **283**(40): p. 26948-55.
18. Holden, H.M., I. Rayment, and J.B. Thoden, *Structure and function of enzymes of the Leloir pathway for galactose metabolism.* J Biol Chem, 2003. **278**(45): p. 43885-8.
19. Rempel, A., et al., *Glucose catabolism in cancer cells: amplification of the gene encoding type II hexokinase.* Cancer Res, 1996. **56**(11): p. 2468-71.
20. Wilson, J.E., *Isozymes of mammalian hexokinase: structure, subcellular localization and metabolic function.* Journal of Experimental Biology, 2003. **206**(12): p. 2049-2057.
21. Timson, D.J. and R.J. Reece, *Functional analysis of disease-causing mutations in human galactokinase.* European Journal of Biochemistry, 2003. **270**(8): p. 1767-1774.
22. Sullivan, M.R., et al., *Quantification of microenvironmental metabolites in murine cancers reveals determinants of tumor nutrient availability.* eLife, 2019. **8**: p. e44235.
23. Reinfeld, B.I., et al., *Cell-programmed nutrient partitioning in the tumour microenvironment.* Nature, 2021. **593**(7858): p. 282-288.
24. Meiser, J., et al., *Serine one-carbon catabolism with formate overflow.* Sci Adv, 2016. **2**(10): p. e1601273.
25. Benzarti, M., et al., *Metabolic Potential of Cancer Cells in Context of the Metastatic Cascade.* Cells, 2020. **9**(9).

26. Hyroššová, P., et al., *PEPCK-M recoups tumor cell anabolic potential in a PKC-ζ-dependent manner.* Cancer Metab, 2021. **9**(1): p. 1.
27. Keshet, R., et al., *Targeting purine synthesis in ASS1-expressing tumors enhances the response to immune checkpoint inhibitors.* Nature Cancer, 2020. **1**(9): p. 894-908.
28. Leithner, K., et al., *PCK2 activation mediates an adaptive response to glucose depletion in lung cancer.* Oncogene, 2015. **34**(8): p. 1044-50.
29. Vincent, E.E., et al., *Mitochondrial Phosphoenolpyruvate Carboxykinase Regulates Metabolic Adaptation and Enables Glucose-Independent Tumor Growth.* Mol Cell, 2015. **60**(2): p. 195-207.
30. van der Reest, J., et al., *Proteome-wide analysis of cysteine oxidation reveals metabolic sensitivity to redox stress.* Nature Communications, 2018. **9**(1): p. 1581.
31. Yang, C., et al., *Glutamine oxidation maintains the TCA cycle and cell survival during impaired mitochondrial pyruvate transport.* Mol Cell, 2014. **56**(3): p. 414-424.
32. Lyssiotis, C.A. and A.C. Kimmelman, *Metabolic Interactions in the Tumor Microenvironment.* Trends in Cell Biology, 2017. **27**(11): p. 863-875.
33. Hui, S., et al., *Glucose feeds the TCA cycle via circulating lactate.* Nature, 2017. **551**(7678): p. 115-118.
34. Faubert, B., et al., *Lactate Metabolism in Human Lung Tumors.* Cell, 2017. **171**(2): p. 358-371.e9.
35. Cheung, S.M., et al., *Lactate concentration in breast cancer using advanced magnetic resonance spectroscopy.* British Journal of Cancer, 2020. **123**(2): p. 261-267.
36. Leithner, K., et al., *The glycerol backbone of phospholipids derives from noncarbohydrate precursors in starved lung cancer cells.* Proceedings of the National Academy of Sciences, 2018. **115**(24): p. 6225-6230.
37. Buescher, J.M., et al., *A roadmap for interpreting (13)C metabolite labeling patterns from cells.* Curr Opin Biotechnol, 2015. **34**: p. 189-201.
38. Lemaigre, F.P. and G.G. Rousseau, *Transcriptional control of genes that regulate glycolysis and gluconeogenesis in adult liver.* Biochem J, 1994. **303 (Pt 1)**(Pt 1): p. 1-14.
39. Kano, A., T. Iwasaki, and M. Shindo, *Bongkrekic acid facilitates glycolysis in cultured cells and induces cell death under low glucose conditions.* Biochemistry and Biophysics Reports, 2019. **20**: p. 100683.
40. Anastasiou, D., et al., *Pyruvate kinase M2 activators promote tetramer formation and suppress tumorigenesis.* Nat Chem Biol, 2012. **8**(10): p. 839-47.
41. Weinstabl, H., et al., *Intracellular Trapping of the Selective Phosphoglycerate Dehydrogenase (PHGDH) Inhibitor BI-4924 Disrupts Serine Biosynthesis.* J Med Chem, 2019. **62**(17): p. 7976-7997.
42. Smith, G.K., et al., *Activity of an NAD-dependent 5,10-methylenetetrahydrofolate dehydrogenase in normal tissue, neoplastic cells, and oncogene-transformed cells.* Arch Biochem Biophys, 1990. **283**(2): p. 367-71.
43. Lorenz, N.I., et al., *AMP-kinase mediates adaptation of glioblastoma cells to conditions of the tumour microenvironment.* bioRxiv, 2022: p. 2022.03.25.485624.
44. Fan, J., et al., *Quantitative flux analysis reveals folate-dependent NADPH production.* Nature, 2014. **510**(7504): p. 298-302.
45. Bichi, R., et al., *Human chronic lymphocytic leukemia modeled in mouse by targeted TCL1 expression.* Proc Natl Acad Sci U S A, 2002. **99**(10): p. 6955-60.
46. Chakraborty, S., et al., *B-cell receptor signaling and genetic lesions in TP53 and CDKN2A/CDKN2B cooperate in Richter transformation.* Blood, 2021. **138**(12): p. 1053-1066.
47. Chaneton, B., et al., *Serine is a natural ligand and allosteric activator of pyruvate kinase M2.* Nature, 2012. **491**(7424): p. 458-462.
48. Ye, J., et al., *Pyruvate kinase M2 promotes de novo serine synthesis to sustain mTORC1 activity and cell proliferation.* Proceedings of the National Academy of Sciences, 2012. **109**(18): p. 6904-6909.
49. Rossi, M., et al., *PHGDH heterogeneity potentiates cancer cell dissemination and metastasis.* Nature, 2022. **605**(7911): p. 747-753.
50. Muir, A. and M.G. Vander Heiden, *The nutrient environment affects therapy.* Science, 2018. **360**(6392): p. 962-963.

51. Zheng, Y., et al., *Mitochondrial One-Carbon Pathway Supports Cytosolic Folate Integrity in Cancer Cells.* Cell, 2018. **175**(6): p. 1546-1560.e17.
52. Kiweler, N., et al., *Mitochondria preserve an autarkic one-carbon cycle to confer growth-independent cancer cell migration and metastasis.* Nat Commun, 2022. **13**(1): p. 2699.
53. Hiller, K., et al., *MetaboliteDetector: comprehensive analysis tool for targeted and nontargeted GC/MS based metabolome analysis.* Anal Chem, 2009. **81**(9): p. 3429-39.
54. Wang, T., et al., *Inosine is an alternative carbon source for CD8(+)-T-cell function under glucose restriction.* Nat Metab, 2020. **2**(7): p. 635-647.
55. Dranka, B.P., et al., *Assessing bioenergetic function in response to oxidative stress by metabolic profiling.* Free Radic Biol Med, 2011. **51**(9): p. 1621-35.